

Deformation Mechanisms of Zinc Single Crystal Investigated with Spherical Nanoindentation Test



STANISŁAW KUCHARSKI, VIET NGHIA DOAN, and MICHAŁ MAJ

Pure Zinc single crystal was examined with instrumented spherical indentation on the basal-oriented surface with different tips' radii. Atomic force microscopy (AFM) and electron backscatter diffraction (EBSD) were used to investigate the topography and orientation changes within the imprint and the surrounding surface. Noticeable pop-ins were reproducible in the majority of tests. Contrary to the literature reports on zinc, plastic deformation was observed prior to the first pop-in, resulting in a hysteresis between loading and unloading curves. Therefore, pop-ins were associated not with the onset of plastic deformation but with slip deformation and contraction twinning because the twins were found inside and outside the imprint after pop-in event. Numerous cells with different orientations resulting from slip and twinning were revealed by EBSD analysis of the residual impressions. The external twins manifested as sink-in patterns. To illustrate the experimental observations, schemes for the evolution of the complex pile-up/sink-in pattern in terms of the parameters of the pop-in event and the increase of the load after the pop-in event have been proposed. Some novel aspects of Zinc nanoindentation were observed including pop-in bursts occurred during unloading process and detwinning properties after indentation. Finally, the difference between indentation results corresponding to two different tips, including the inverse size effect in the indentation phase prior to the pop-in event, was briefly discussed.

<https://doi.org/10.1007/s11661-025-07820-6>
© The Author(s) 2025

I. INTRODUCTION

ZINC and Magnesium are the metals that have a hexagonal close packed structure (HCP) and both were used to investigate this crystal structure. The mechanical testing of zinc can be divided into two groups: the first involves applying a nominally uniaxial stress state (such as uniaxial tension^[1] and compression^[2-4]), and the second involves performing indentation tests. In the first group, the fundamental mechanical properties (sequence of slip or twin systems activation, critical resolved shear stress) can be identified, while in the second group, the multiaxial stress state occurs and more advanced deformation mechanisms can be studied.

Interest in the research and development of macro- and nanoscale^[5-9] testing of zinc has grown significantly in the last few decades, thanks to advancements in characterization technology. For soft materials such as zinc, instrumented indentation techniques have increasingly been applied for examinations at small scales.

However, to the best of the authors' knowledge, only a handful of studies have contributed to the data on nanoindentation of pure Zinc. The majority of studies of zinc has been done in quasi-single crystal (in center of very large grains, far from grain boundary).

Much effort was dedicated to examining properties and deformation properties of zinc when indented in different crystal orientations. Creeping behavior of zinc in nanoindentation was investigated in^[10,11] Zinc elastic modulus was experimentally calculated in^[10-12,15] for basal, prismatic, and pyramidal oriented grains. The nanoindentation tests in Zinc grains having different orientations were carried out by Nguyen *et al.*,^[13] using a sphero-conical tip (radius 1 μm), for the maximum depth and load of 250 nm and 1 mN, respectively. The tests were simulated using crystal plasticity model. It was assumed that basal, prismatic, 2nd-order pyramidal slip and compression twin systems were active in the test. This approach was applied to study the effect of cold rolling on nanoindentation response of Zinc.^[14] It was concluded that the resolved shear stress increases with reduction of thickness in cold rolling process.

The deformation mechanism of zinc was more explored by Sarvesha *et al.* in^[15] using spherical indentations, along with AFM and EBSD analysis of residual impressions. The tip used had the radius $R = 10 \mu\text{m}$ and the load of 100 mN was applied, which corresponds

STANISŁAW KUCHARSKI, VIET NGHIA DOAN and MICHAŁ MAJ are with the Institute of Fundamental Technological Research, 02-106 Warsaw, Poland. Contact e-mail: skuchar@ippt.pan.pl
Manuscript submitted October 24, 2024; accepted May 4, 2025.

to $h/R = 0.3$ to 0.4 . For indentation in (0001) direction, a pile-up with quasi regular hexagonal shape was observed, while for other indentation directions (pyramidal, prismatic), the pile-up and sink-in in a form of characteristic cross-sectional valley was generated. At the bottom of imprints, fragmentations of grain and generation of sub-grains were noticed in the orientations away from basal. Indentation in the basal plane was associated with the stiffest P - h curves and the lowest pile-up resulting from second-order pyramidal slip which exhibit high strain hardening. The basal slip was also activated; however, unlike other indentation on non-basal planes, the presence of twins was not observed. The deformation modes were discussed for indentation on pyramidal and prismatic planes.

Compared to Magnesium, Zn shows a strong anisotropy in its elastic and plastic properties and demonstrates different deformation mechanisms due to its higher (c/a) ratio of 1.856.^[16] Therefore, the response of Magnesium in mechanical tests is different than that of Zinc; however, a brief overview of articles on Mg highlights some areas of interest in the mechanical testing of HCP metals. In many papers, indentation was used to identify critical resolved shear stress (CRSS) for different slip or twinning systems in Mg. To this end, the indentation stress-strain curves were extracted from load-displacement data.^[17] From the Yield stress (onset of plasticity), which is visible on P - h curves, the CRSS was calculated using Hertz equations and Schmidt factor. Nayyeri *et al.* have shown that CRSS identified from indentation stress-strain curve strongly depends on tip radius and this is a manifestation of size effect.^[18] Tips with different radii in the range of 1 to 250 μm were applied. The authors associated discontinuities on the unloading curve with detwinning process, which depends on tip radius. Similar approach was applied in^[19] to identify CRSS for basal slip in polycrystalline magnesium alloys. The same series of tips (radii 1 to 250 μm) were applied in indentation tests of Mg alloys grains with different angles between indentation direction and c -axis direction (10 deg, 50 deg and 80 deg). It was observed that for some alloys, smaller tip radii lead to the activation of slip systems other than those activated by larger radii, and the relationship between $R^{-1/2}$ and indentation CRSS is not linear.

The identification of CRSS using methodology based on Berkovich indentation of differently oriented grains combined with crystal plasticity simulation was proposed by Sanchez *et al.*^[20] The Mg alloys were examined using indentation test with 5 μm radius spherical tip.^[21] The initial yield point detected on load-displacement curve corresponded to basal slip, while subsequent pop-in event was associated with twinning. CRSS corresponding to slip and twinning was identified. In numerical simulations with CPFEM,^[22] the effect of indentation direction and indenter radius on twin initiation in magnesium was shown. The CRSS values were determined from comparison of numerical and experimental load-displacement curves. The sharp indentation of different orientations of magnesium single crystal was analyzed numerically (cono-spherical tips) and experimentally (cube corner tip) by Somekawa

et al.^[23] It was observed that $\{10\bar{1}2\}$ type twins for both basal and prismatic indentation directions were formed independently of temperature, and this type of twin was promoted by a sharper indenter tip.

Somekawa *et al.*^[24] investigated also the incipient plasticity in magnesium during nanoindentation test with tip of small radius (0.35 μm). For indentation on the basal plane, a higher pop-in load and larger pop-in width was observed than for the prismatic plane. This was due to the activation of pyramidal dislocations (which required higher energies) during indentation on the basal plane. On the other hand, in the early stages of indentation on the prismatic plane, basal dislocation activity was observed, which required lower energies.

Kitahara *et al.*^[25] presented numerical and experimental study of microindentation tests (tip radius 500 μm), of magnesium single crystal. During indentation on basal plane, the basal and pyramidal slip systems were activated, while indentation on (1 $\bar{1}$ 00) and (11 $\bar{2}$ 0) planes yields activation of basal slip and twin systems. Using simulations with CPFEM, they clarified how interaction of these two systems influences the topography of residual impressions and microstructure generated beneath the indents.

The indentation test with conical tip (tip radius 1 μm , penetration depth up to 22 μm) on single grains of magnesium having different orientation was conducted by Zambaldi *et al.*^[26] Different twin variants were identified on the samples surface using EBSD, and analysis of twinning strains and residual impressions topography (confocal microscopy) was performed. The twin patterns had mostly reproducible lamellar fashion and were correlated with indentation direction. From the comparison of experimental and numerical simulations results (CPFEM), it was concluded that an improved modeling is required.

During load-controlled nanoindentation experiments, a phenomenon characterized by a sudden burst of displacement, or “pop-in,” is often observed. A widely accepted school of thought regarding the origin of the pop-in is that it is due to dislocation nucleation in the highly stressed region below the indenter.^[27-29] In this regard, the pop-in will act as a trigger for the onset of permanent deformation, and prior to this excursion, the material has totally elastic behavior. Nevertheless, this aspect of nanoindentation is not well explored or documented for zinc, as the pop-in event is either absent or contributes little displacement in experiments, leading to the inability to further study this phenomenon with numerical models.

The pop-in events of zinc were examined by Catoor *et al.*^[30] for indentation tests with 3.3 μm tip on (0001), (10 $\bar{1}2$) and (10 $\bar{1}0$) planes. The slip on basal plane was indicated as the most likely deformation mechanism, twinning was observed for indentation on the prismatic plane and not for the basal plane. The highest pop-in loads were observed for (0001) plane. The cumulative probability of pop-in events was presented. Tension twins and lack of compression twins were observed.

In this study, single-crystal zinc was investigated using nanoindentation with spherical tips of 1.75 and 9.2 μm

radius giving moderate deformation (depth/radius ratio, $h/R = 0.1$ to 0.15). We examine pristine material (after annealing and etching) to show pristine deformation mechanisms, since even small amounts of cold work can alter the sequence of slip system activity.^[9] Due to careful sample surface preparation, we observed significant pop-in events in the majority of the nanoindentation tests, which has rarely been reported in the literature for Zn. To reveal the deformation mechanisms, we measured the topography of the residual indentations using AFM and the changes in crystallographic orientation using EBSD. The pop-in bursts were registered, categorized, and correlated with a specific pile-up/sink-in pattern and with the formation of small crystallographic cells in the residual impressions. Some aspects of indentation size effect were discussed. An underlying deformation mechanism of Zinc indentation was formulated based on the experimental results.

II. EXPERIMENTAL DETAILS

It has been observed in numerous studies that the likelihood of pop-in event occurrence is dramatically reduced by altering the surface mechanically,^[31–33] or as Pathak et al.^[34–36] phrased it in their research, the pop-in can be “avoided” by tampering the surface with mechanical means. Even miniscule degree of mechanical polishing with vibratory method can be detrimental to the observation of pop-ins, and traditional mechanical polishing with grit paper could potentially eliminate the opportunity entirely. A common explanation for this is given as, conventional mechanical polishing introduces dislocations or damage to the near-surface structure, plastic deformation can utilize this source of available defects rather than nucleation of new ones to manifest. The result is a smooth transition without significant interruption on indentation P - h curve. Tests under this uncontrollable condition may not reflect the intrinsic characteristics of materials, especially for pure metal samples. Therefore, it is imperative to pursue a surface preparation method that induce as little stress to the surface as possible, which is presented in the next paragraph.

High-purity (99.9999 pct) Zinc single-crystal material, produced by the Czochralski method, in the form of a rod of 14 mm in diameter was acquired from MaTecK GmbH (Germany). The rod axis was parallel to the c -axis of the crystal. The rod was cut into smaller samples of ~ 5 mm in height, perpendicularly to the rod axis, by a wire saw in order to minimize the damage done to the material and to obtain a relatively even surface. To lessen the potential dislocations induced by the previous cutting process, samples were annealed at 200 °C for 2 hours, heating rate was 5 °C/minute and then cooled down in furnace. The effect of annealing process on the presence of pop-in event was shown by Miller et al.^[37] for thin gold films. In the authors’ study, pop-ins were observed for annealed samples, but not for as-deposited specimen. Electropolishing was used as to reduce the roughness on surface. The electrolyte we found the most success with was a solution of chromic

acid and distilled water. The surface was examined with light microscope and atomic force microscope for flat areas of reasonably large size and mean roughness S_a of 2 to 10 nm in our research. The samples were preserved in a desiccator between experiments.

The UNHT tester (Anton Paar, Open Platform, equipment,) was used to perform the nanoindentation tests and returned results in form of load-penetration curves. The nanoindentation tests were performed using two types of tip radii: $R = 1.75$ μm and $R = 9.2$ μm . The calibration of the tips was done previously in.^[38] The maximum registered depth for the system is $h = 50$ μm and the load range is $F = 0$ to 50 mN. The displacement and load resolution are 0.0005 nm and 2.5 nN, respectively. All of the tests were performed in load-controlled mode. The NanitAFM (Nanosurf AG, Switzerland) atomic force microscope (AFM) was used to scan residual imprints after nanoindentation tests. The 3D (XYZ) maps of the imprints typically produced by AFM were additionally analyzed using Gwyddon software, and the gradients of the measured surfaces were specified. By presenting the surface in terms of its gradients, we reveal some features, such as small areas with different slopes and different heights, which manifest themselves as a small step at a common boundary. In particular, the boundary of the sink-in and the contact boundary between the indenter and the specimen are visible.

For tests with tip radius $R = 1.75$ μm , loading and unloading speed were 2.0 and 2.5 mN/minute, respectively. While for tests with $R = 9.2$ μm , the chosen parameters were 20 and 20 mN/minute. A holding time between loading and unloading of 2 s was applied for all tests. The contact was detected with an indenter force sensor, and the applied load was 0.005 to 0.001 mN. The maximum load was adjusted so that the relative depth of penetration h/R was in the range of 0.1 to 0.15 (not precisely defined due to random character of pop-in length). The basal, (0001), plane was indented. For each indenter tips and tested loads, the experiments were repeated on different samples to verify the repeatability of the results, particularly for the loading portion of the P - h curve prior to the first pop-in event, taking into account scattering of pop-in load and length results. The imprints are labeled by the following method: R9 and R1.75 to denote the tip sizes used of 9.2 μm and 1.75 μm , respectively; the next combination of letter and number to denote the time at which the experiment took place; the final number is the specific indent in the experiment.

The evolution of crystallographic orientation after the indentation tests was analyzed using the Electron Backscatter Diffraction (EBSD) method with a Zeiss CrossBeam 350 Scanning Electron Microscope equipped with a Hikari Super EBSD camera. The analyses were performed with an acceleration voltage of 22 kV and a beam current 2.2 nA. All EBSD maps were collected with a 40 nm step size.

III. RESULTS

A. Nanoindentation Tests: Load–Displacement Curves and Residual Impression Topography

The pop-in events were usually observed in the nanoindentation tests of single crystals and the intensity of these phenomena depends on the density of defects in the examined material. In the examined zinc single crystal, the defect density was reduced by annealing; therefore, the pop-in was present in almost all tests. In our analysis of pop-in events, we refer to those with long displacements (tens of nanometres). Very short pop-ins (single nanometres) are not discussed because, given the radius of our tip, they may result from the flattening of a single asperity in the contact process.

When the applied load exceeds the pop-in initiating load, the indentation tests in zinc can be classified accordingly to the position of pop-in burst on the loading–unloading curve. Typically, the pop-in event occurs most frequently at a certain load range and may appear on the loading and/or unloading curve, and rarely during the holding time. In the latter case, the pop-in bursts, which occurred in a very short time (small fraction of second), begin during the holding window (it was set to about 2 seconds) in the indentation process. After the pop-in event, the imprints were still within the holding time and would continue to be under load before unloading process. According to the recorded diagrams, the imprints were under an almost constant load level during the short pop-in time period; however, the actual load may fluctuate and the fluctuations were only roughly registered due to instrument inertia.

The distinct double pop-in, *i.e.*, the one burst occurs during loading and the second during unloading or two bursts on the loading curve are also possible; however, this type of pop-in event is rarely observed. In each of the above cases, one can observe different lengths of the pop-in burst which can indicate different deformation modes.

In many publications about the indentation of HCP single crystals, the pop-in events are associated with generation of twins, *e.g.*,^[18,30]

In this paper, we present results of AFM measurements and EBSD analysis of residual imprints, and we show that the surface and bottom twins occur when the imprint exhibited a specific topography, *i.e.*, the pile-up with the cross-sectional valley (sink-in). This topography is also visible with light microscopy. We analyzed a correlation between pop-in initiation load, pop-in length, pile-up/sink-in pattern, and the presence of twins.

1. Tests with 9.2 μm radius tip

As with other metals, for Zn, the loading curve changes significantly when the pop-in event occurs. The first pop-in is widely accepted as the onset of permanent deformation during nanoindentation.^[39,40] For such reason, if the unloading starts at a load lower than the pop-in initiating load, the unloading curve should coincide with the loading one. To verify this condition, we conducted a number tests with FCC metals (Cu, Ni),

and it was fulfilled. However, for zinc, we have observed a difference between loading and unloading curve, *i.e.*, small hysteresis loop and a small residual penetration depth remain after the test with the 9.2 μm tip, Figure 1.

This small residual depth was examined using AFM technique revealing that it is greater than the surface roughness, indicating that this is not simply flattening the roughness, but the material exhibits a very small level of plastic deformation instead of the expected pure elasticity. This is confirmed by comparison with theoretical, elastic Hertz curve, which lays above the experimental curves in the whole range of penetration depth. The small irregularities on the curve at around 60 nm depth can be considered as a manifestation of slip evolution rather than the onset of plastic deformation.

This occurrence is rarely observed in experiments, but nonetheless was reported by other researches.^[18,19,41,42] Other groups^[43,44] have also confirmed the dislocation activity prior to the onset of the first pop-in at low penetration depth. Maughan *et al.*^[45] proposed several stages of deformation to explain the early phase of the indentation process and indentation size effect. These stages are related to the stacking fault energy (SFE) and the dislocation structure present in the material. In the reference,^[46] the authors presented a range of behavior for several materials, from fully elastic to plastic, in low maximum load indentation tests. This variation was found to exist despite the presence of mobile dislocations at the indentation location and was attributed to different microstructural states and/or surface features. Schuh^[39] also remarked that the nominally fitted portion of the P – h curve to Hertzian contact theory would contain some degree of undetectable plastic deformation. This hysteresis can be explained by Zinc that has a rather low melting temperature; thus, slip systems may be more easily thermally activated at room temperature.^[6]

Nevertheless, the possibility of a thin film of oxide formed on the surface (from the electropolishing surface preparation method) is cause of this hysteresis that cannot be ruled out as demonstrated by Chiu *et al.*^[47]

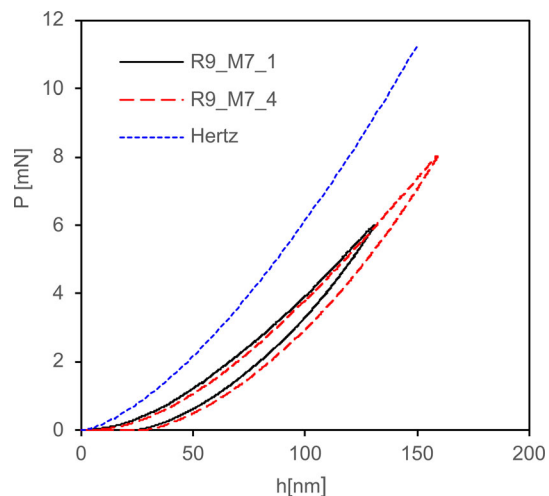


Fig. 1—Comparison of Hertz curve with loading–unloading curves for applied forces lower than pop-in load.

They reported a thin film of 17 nm nickel chloride after their electropolishing experiment was the cause for the deviation between loading and unloading curve in the P - h curve prior to the first pop-in.

In our experiments, we estimated the effect of oxides by comparing indentation results over several days. We have observed that the material response changes (probably due to oxides), when the time between the etching and the test increases, although the samples were kept in desiccator vessel. Therefore, we conducted indentation in the first 1 to 2 days after etching, since for this period, the results were fully repeatable; subsequently, it is assumed that during this time, the possible growth of the oxides layer was insignificant. Our assumption that the effect of oxides was not important was also confirmed indirectly by EBSD analysis. The number of non-indexed points increased with time between etching and measurement, and was low for “freshly” etched samples (no later than 2 to 3 days after etching), indicating that their surface was only slightly contaminated by oxides.

The knowledge if plastic deformation is present before the pop-in is important when the contact stress corresponding to the pop-in initiating load has to be calculated. Usually the pop-in stress is calculated on the basis of the assumption that prior to pop-in we have purely elastic deformation. It is not a case for zinc, c.f. Figure 1.

The majority of curves were found to contain distinct pop-ins with distribution of statistical nature. For the tests that showed a longer pop-in, a specific pile-up/sink-in pattern has been observed by light microscopy and AFM. In the test without pop-in, the pile-up/sink-in pattern was not detected. In some tests, however, the pop-in displacements are very small and they manifest as discontinuities on the P - h curve. Different types pop-in curves are presented in Figure 2.

In order to analyze the deformation mode of the Zn single crystal in the indentation tests, specific topography of the residual imprints should be considered. In isotropic materials, the shape of residual impression depends on strain hardening of the examined material, the pile-up pattern appears when material exhibits low strain hardening and the sink-in pattern corresponds to high strain hardening. In single crystals, the response of material is more complex, *i.e.*, due to material anisotropy, alternate sink-in and pile-up around the indent can be observed, and the pattern depends on crystal symmetry, *e.g.*,^[15,26,48] For example, in FCC crystals, for the indentation in 001 direction, there is a fourfold symmetry of the imprint, with pile-up in [011] directions and sink-in in [100] and [010] directions. The pile-up pattern does not depend on the pop-in event and indentation twins do not occur.^[38]

The complex shape of pile-up patterns for Zn single crystal is presented below in Figures 3, 4, 5, 6, and 7. In Figure 3, we present a map and three cross-sectional profiles of the imprint R9_O17_11 [P - h curve in Figure 2(a)]. One observes a long valley across the pile-up around the imprint and both form a specific topography, described by Sarvesha *et al.*^[15] as a hillock and bird wing, giving a very complex shape to the

contact boundary. A certain proportion, about 2/3 (or 4/6) of the circumference surrounding the imprint, shows a pile-up, while the remaining part forms a sink-in (long valley), Figure 3. The difference between the lowest point of the contact boundary and the highest point of the contact boundary is called t . We refer to this shape of residual impression as a “pile up/sink-in” pattern. The material response for a majority of indentation tests conducted in our research with 9.2 μm radius tip and different loads, Figure 2(a), is qualitatively similar to that described above, Figure 3.

Other possible shapes of residual impression, although rather rarely observed, are presented in Figure 4. In the case of indent without pop-in event, test R9_O17_2, Figure 2(a), as the load continued to reach the maximum value of 36 mN, (the load required to achieve to ratio h/R of 0.11), the residual impression is shown to have hexagonal pile-up formation, Figure 4(a). This behavior is similar to that reported in other studies regarding HCP materials in basal plane.^[15,30] For pop-in events that occur at low load (4 to 5 mN), and the maximum load is low, 8 to 10 mN, test R9_O17_14, R9_M7_6, Figure 2(b), the residual impression examined by AFM measurement to be without pile-up or sink-in; in other words, it is a flat surface in all directions, Figure 4(b). However, when the second pop-in occurred on the loading curve that corresponds to the greater load (8.29 mN, R9_F10_11, Figure 2(b), after the first pop-in initiated at lower load, the residual impression changes with the generation of the sink-in/pile-up pattern, Figure 4(c). The result is similar to the most common response presented in Figure 3. The existence of the second pop-in event could be correlated to the generation of the pile-up/sink-in pattern.

While the values of the pop-in initiating load and the pop-in length are rather random, they can be correlated with the shape of residual impression. From the length of the pop-in and its position on the P - h curve, one can estimate a particular topography of the pile-up/sink-in pattern. From many tests, selected sets of examples were chosen to show the influence of these parameters on residual impression's topography.

The first set consists of imprints with similar pop-in load level and different maximum loads. Imprint R9_N15_5, Figure 5(a), which has the first pop-in event at a slightly greater load (~ 8 mN) and maximum load of 36 mN (P - h curve shown in Figure 2(c), is observed to have the pile-up in hexagonal shape not too dissimilar from that shown for R9_O17_2, Figure 4(a). However, the residual impression is not completely surrounded by the pile-up formation, and there is a small gap that can be detected. The profile for the gap is provided on the right (profile 1) and shows that it is not in form of sink-in, and its height corresponds to the non-deformed surface. The presence of a relatively long pop-in could contribute to the appearance of this gap, or the lack of pile-up in one specific direction.

For a similar load-penetration curve, R9_N15_4, Figure 2(c), the trace of sink-in is more distinct, Figure 5(b). This can be associated with several small secondary pop-ins, which are present on the curve

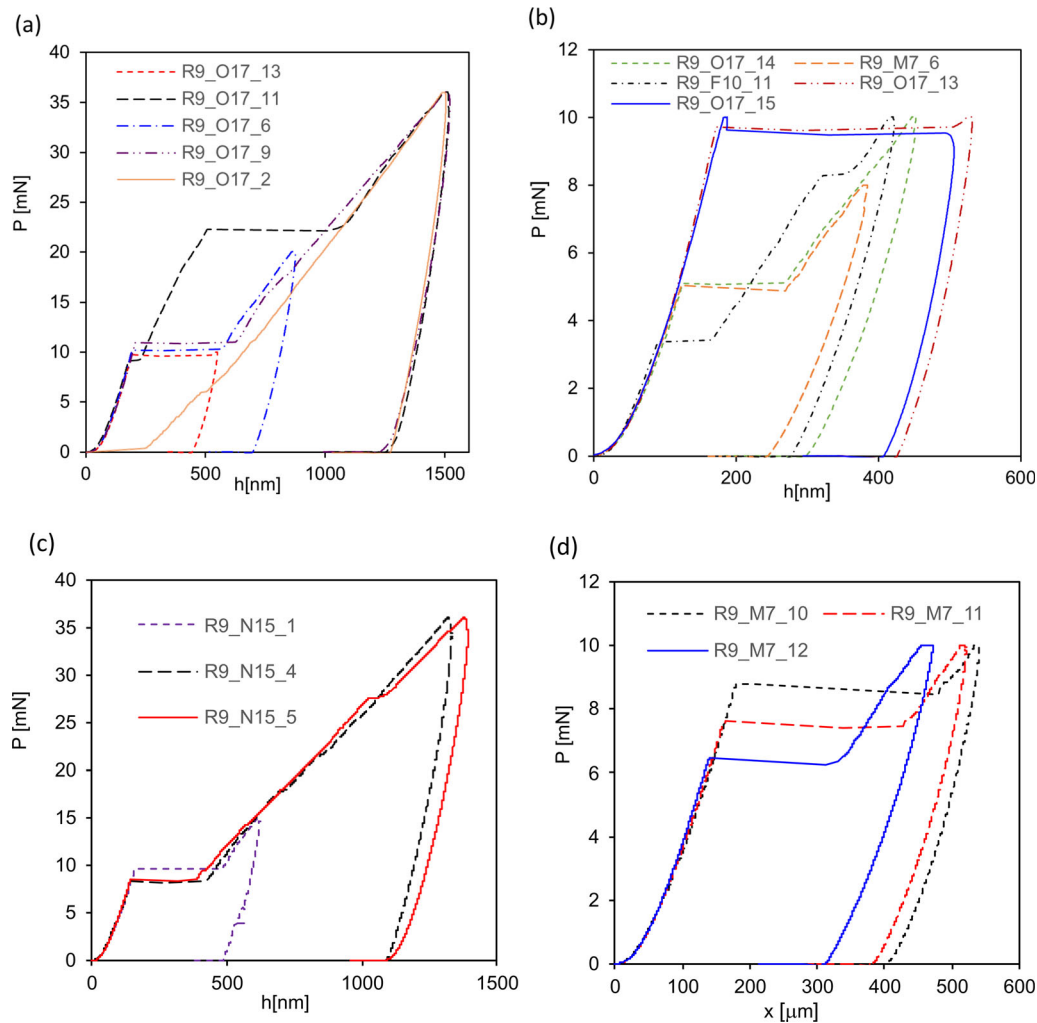


Fig. 2— P - h curves presented for different cases: (a) typical P - h curves and two outliers, one with very long pop-in (R9_17_11) and the other without pop-in at high maximum load (R9_17_2); (b) imprints that have pop-in event during unloading, very close to maximum load, and low pop-in load; (c) imprints that have the similar pop-in load but different residual impressions; (d) imprints with similar maximum load but different pop-in load.

R9_N15_4, while on the curve R9_N15_5, only one secondary pop-in close to the maximum load is visible. The relatively small increase of pop-in initiating load, from 8 to 9.5–10 mN, and lower maximum load, which is closer to the pop-in initiating load, test R9_N15_1, Figure 2(c), or R9_O17_13, Figure 2(b), may lead to important change of the pile-up pattern where a distinct sink-in appears, Figures 5(c), (d) respectively. We observed that for a fixed pop-in initiating load, the cross-sectional valley is most distinct when the maximum loading was only slightly increased after the pop-in, imprint R9_O17_13, Figure 5(d).

The other set of imprints examined had a maximum load of 10 mN, but the initiation of pop-in took place at different levels of load, Figures 2d and 6. The pop-in loads for tests R9_M7_10, R9_M7_11, and R9_M7_12 were 8.79 mN, 7.65 mN, and 6.48 mN, respectively. The first test in this set had the most pronounced pop-in event and its imprint was most similar to that shown in Figure 3; however, it had an additional attribute, and the outer shape of the pile-up was quasi-hexagonal

Figure 6(a). We observe that as the difference between pop-in level and maximum load increases, the imprint (R9_M7_11) is still similar to that presented in Figure 3; however, the pile-up height is smaller, and sink-in is shallower than for the imprint R9_M7_10 and becomes more difficult to detect the sink-in on the surface, Figure 6(b). Indent R9_M7_12, Figure 6(c) has the smallest pop-in length and pop-in initiating load, and therefore, the greatest load increase after pop-in, this results in a residual impression that shows neither pile-up nor sink-in, presented already in Figure 4(b).

The results presented in Figures 5, 6 indicate that the degree of detectable sink-in is affected by both the load initiating pop-in event and the maximum load. To further examine this effect, another set of indents was chosen including indents R9_O17_13 (or R9_O17_15), R9_O17_6, and R9_O17_9. We can observe the evolution of the imprint topography, Figures 5 and 7, when after pop-in burst at about 10 mN, the loading continues to increase.

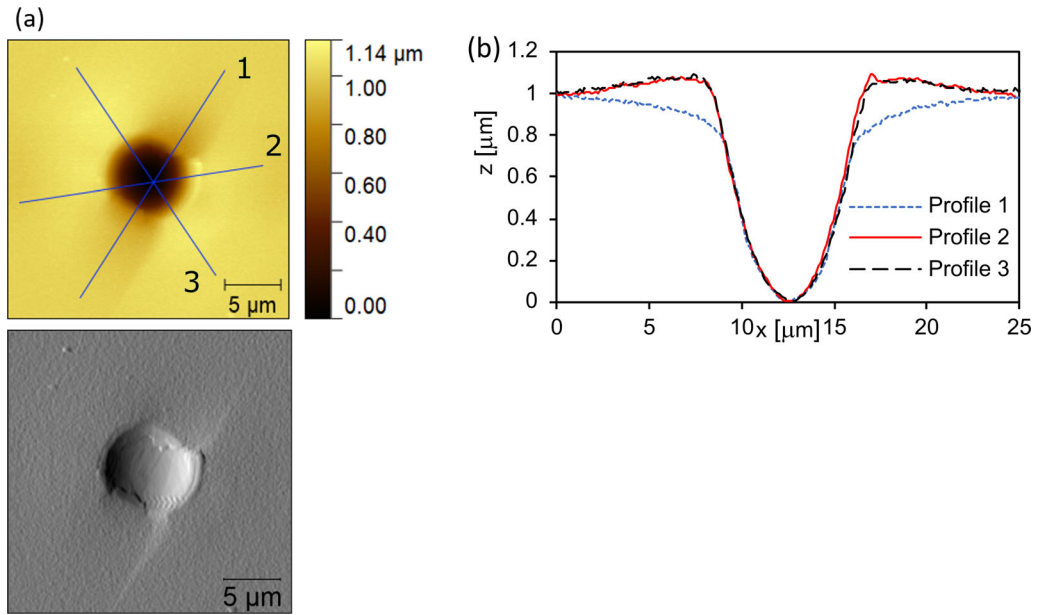


Fig. 3—Surface topography and cross-sectional profiles of imprint R9_O17_11—the most frequently observed residual impression for $R = 9.2 \mu\text{m}$ tests. (a) AFM-measured topography, (b) extracted profiles (Color figure online).

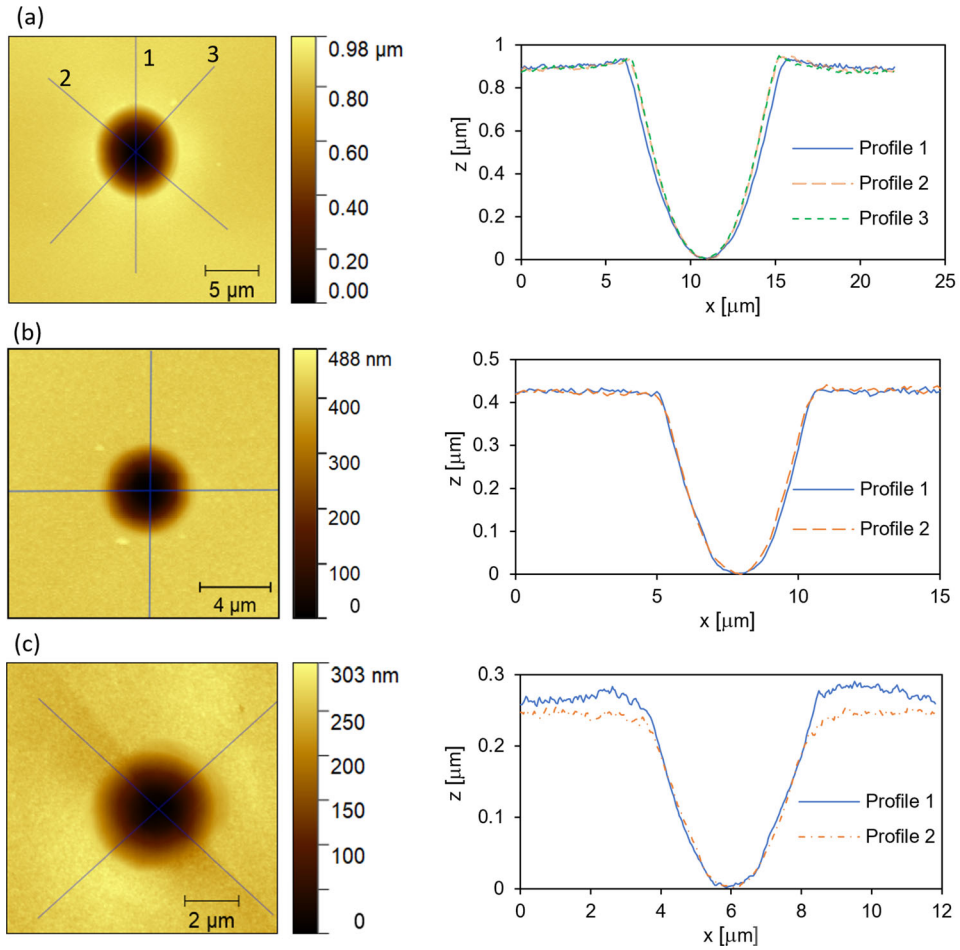


Fig. 4—Surface topography and cross-sectional profiles of imprints that occurs rarely: (a) R9_O17_2—no pop-in, (b) R9_O17_14—low load pop-in, and (c) R9_F10_11—second pop-in at high load.

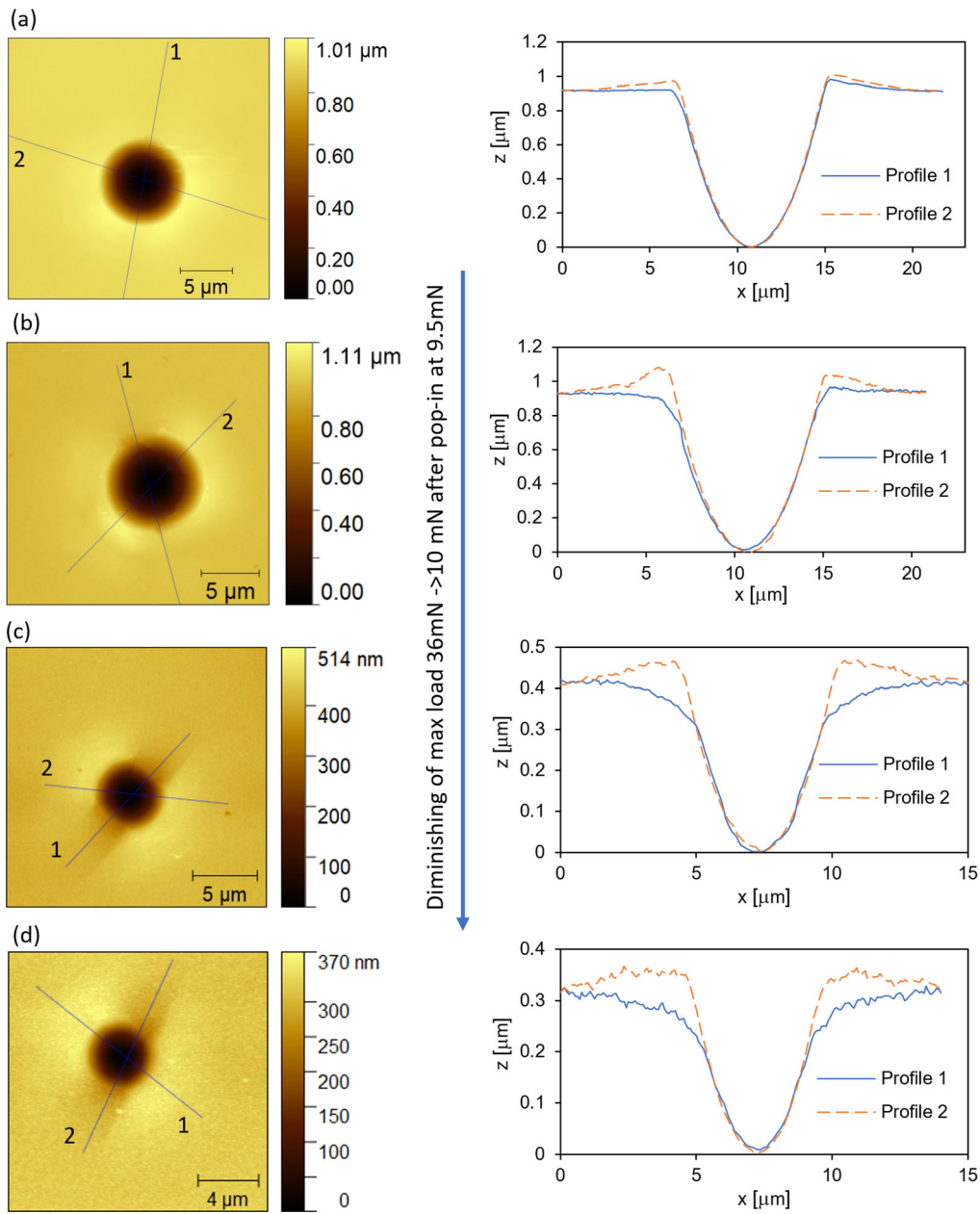


Fig. 5—Surface topography and cross-sectional profiles of imprints: (a) R9_N15_5, (b) R9_N15_4: pop-in load much smaller than maximal load; (c) R9_N15_1, (d) R9_O17_13: pop-in load close to maximal load.

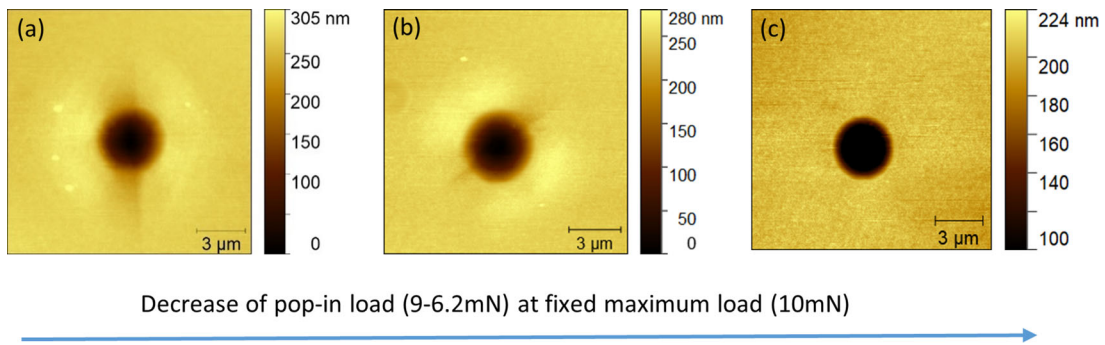


Fig. 6—Surface topography of imprints made with fixed maximum load and diminishing pop-in load (a) R9_M7_10, (b) R9_M7_11, (c) R9_M7_12.

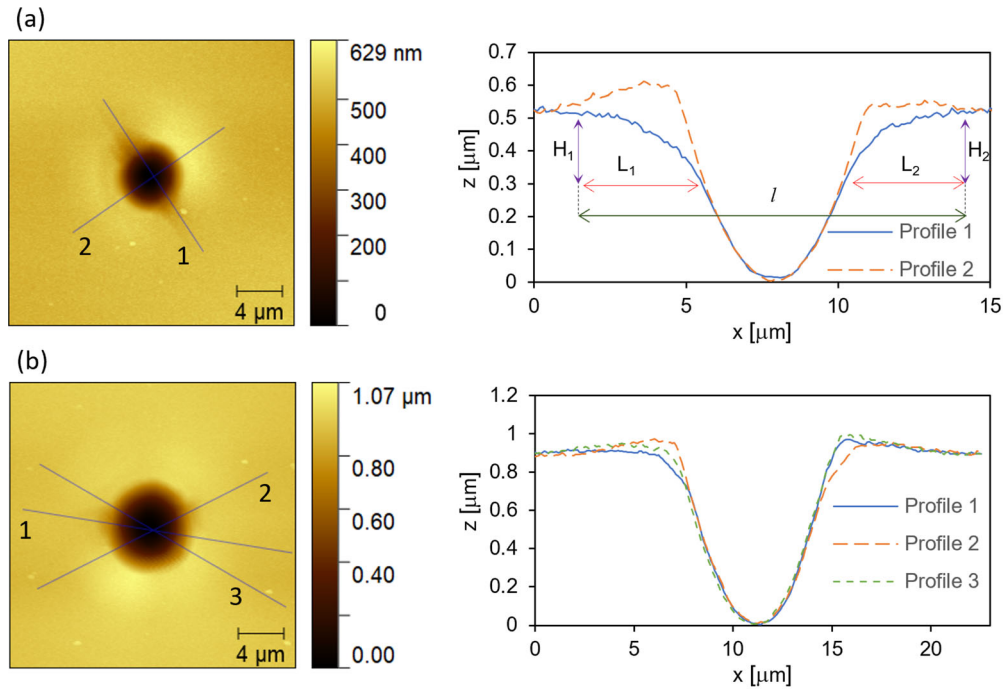


Fig. 7—Surface topography and cross-sectional profiles of imprints made with fixed pop-in load and increasing maximum load. (a) R9_O17_6, (b) R9_O17_9.

The selection of this series is qualitatively similar to that in Figure 5. In both cases, we have a fixed pop-in initiation load and a difference between this load and the maximum load increases, but in this series, the pop-in initiation load is slightly higher.

For indent R9_O17_13, Figure 5(d), pop-in starts at about 10 mN, which is almost maximum load applied in the test, and next, there is unloading. For indent R9_O17_6, Figure 7(a), the pop-in starts at about 10.23 mN but loading is continued up to 20 mN. For the imprint R9_O17_9, the pop-in initiating load (10 mN) was similar to that of the other two, but the loading process was continued up to 36 mN, Figure 7(b). It can be seen that the shape of the sink-in profile changes as the maximum load increases with respect to pop-in load.

To investigate the change of sink-in shape in residual impressions, the following parameters were proposed accordingly to the scheme shown in Figure 7(a):

- $\frac{H}{L}$ —the average of ratio of $\frac{H_1}{L_1}$ and $\frac{H_2}{L_2}$ with H_x and L_x are the depth and length of the sink-in, respectively, on each side.
- P_m —Maximum set load.
- Δ/P_m —Difference between pop-in load and maximum load normalized with respect to maximum load.
- l —The total length of the valley and the indent.

The results are shown in Table I for the chosen imprints and further visualized for all measured indents with sink-in described:

Some information can be gathered from the above data:

- The H/L ratio increases with the increment between pop-in initiating load and maximum load, Figure 8(a).
- The increase of load after pop-in event does not induce the increment in length of sink-in as the l value does not show significant changes, Figure 8(b).
- Indent R9_O17_11 is presented to have typical impression, Figure 3, despite the highest pop-in initiating load, marked in Figure 8. While in Figure 8(a), this indent was not shown to be an outlier for the sink-in shape evolution, it is seen to form a very long sink-in pattern compared to the rest of the results, Figure 8(b). It suggests that the sink-in length shows greater correlation with pop-in initiating load rather than subsequent loading after pop-in, Figure 8(c).
- Long pop-in usually manifests as a sink-in in the residual impression. In the subsequent loading process, the imprint will continue to expand while the sink-in length remains a constant. This expansion will gradually “engulf” the sink-in and this process is more evident for the lower than for the higher pop-in initiating loads c.f. Figures 5, 7. Furthermore, the sink-in shapes are shown to be a straight line or hyperbolic facing upward, H/L ratio should be intuitively a constant value (if the profile is a straight line) or decrease (if the profile has hyperbolic shape) with the increase of load. However, our results show that the ratio increases instead [refer to Figure 8(a) and Table I], suggesting the

sink-in does not simply reduce in length, but also change in shape.

In some cases, although one large pop-in was present on the P - h curve, more than one sink-in were generated, but one of them was distinctly greater, indents R9_N13_8, R9_N14_4, Figure 9. On the P - h curve corresponding to the latter, Figure 9(c), two pop-ins are visible, and the first is much greater than the second. However, the presence of double sink-in is not necessary associated with two pop-ins on P - h curve, since for indent R9_N13_8, we have only single, large pop-in, Figure 9(c).

2. Tests with 1.75 μm radius tip

The typical load-penetration curves of 1.75 μm tip indentation are shown in Figure 10, which are not too dissimilar (qualitatively) to those corresponding to the 9.2 μm tip indent. Discontinuities can be found on the loading curve both prior and after the first pop-in. These interruptions are not identified as “pop-in event” because of their relative minute displacement burst as well as no significant drop in load was registered. The effect of these small interruptions on residual impressions examined with AFM measurement is considered insignificant. Nevertheless, the existence of more than one pop-ins could still be confirmed, similar to that of 9.2 μm tip indentation, but there are some differences between experiments done with each tip. The first dissimilarity is that occurrence of subsequent pop-ins is not limited to the loading process, but also in unloading curve. The second difference is the length of the first pop-in which can be shorter than the following bursts for 1.75 μm tip indentation, while for the larger tip experiment, the first pop-in is observed to be the longer one.

The tests performed with loads lower than pop-in load, *i.e.*, prior to the large pop-in events, were also investigated. The loading portion of the curve is qualitatively similar to the Hertz curve (power law curve); however, the unloading portion does not coincide with the loading one, and elastic recovery is quite miniscule. The residual penetration depth was measured and can be seen to be greater than the mean height of roughness [an example is shown in Figure 11(a)].

This could indicate that, despite the presumably elastic character of the loading curve, a certain amount of plastic deformation accumulates in the sample prior to the pop-in event and the loading-unloading diagram is qualitatively similar to classic P - h curves observed for elastic-plastic polycrystalline metals. The residual impressions corresponding to such tests either without pop-ins, Figure 11(a) or with very short pop-ins length < 60 nm and/or low pop-in load, Figure 11(b) are quite similar, and the pile-ups are hexagonal or circular in shape that do not have significant difference in height in any directions (in form of thin narrow wall), Figure 11. Such behavior may be observed up to the load of about 2 mN and residual depth of about 140 nm.

Pile-up pattern can become more hexagonal at low pop-in load and length as seen in imprint R1.75_N29_3, Figure 12(a), the height of which is homogeneous

(without sink-in) on all sides as observed in Figure 12(b). A possible explanation for this behavior can be given when examining the P - h curve of this imprint, Figure 13. The P - h curve of imprint R1.75_N29_3 shows subsequent pop-in events occurred at higher load and induced larger displacement than the first one, of which effect should be taken into consideration. For comparison, P - h curve of imprint R1.75_D1_12 with circular pile-up (Figure 11) is also shown in Figure 13, the first recorded pop-ins for each imprint are marked with arrows.

The first pop-in of imprint R1.75_D1_12 happened at higher load (2.18 mN) and length (3.8 nm), indicated by the brown arrow, compared to the that of imprint R1.75_N29_3, which has pop-in load and length of 1.52 mN and 2.56 nm, respectively, indicated by the lower gray arrow. Both imprints have similar loading curves up to the first pop-in event of indent R1.75_N29_3. However, imprint R1.75_D1_12 reached maximum load (2.82 mN) shortly after the single pop-in event, while the other imprint had pop-in at the load of 2.54 mN (upper gray arrow), which induced the displacement of about 5.27 nm. The effect of the subsequent pop-in burst requires further investigation. Nonetheless, the existence of more than one major pop-ins could be associated with the differences in residual impressions from those with only one detectable pop-in event. The effects of subsequent pop-ins influencing the shape of residual impressions have also been observed for the $R = 9.2 \mu\text{m}$ tip, as presented in the previous section.

An increase in pop-in length and load would induce more changes to the residual impressions. The pile-up can be seen to become more hexagonal with two sides of the hexagon having reduced height, when pop-in events occur at medium to high load with small induced depth. The examples for this are shown in Figures 14(a), (b) for imprint R1.75_D22_6 and R1.75_F2_8, respectively, whose P - h curves are presented in Figure 13. Both imprints have the maximum load of 2 mN, and R1.75_D22_6 has slightly lower pop-in load and length at 1.9 mN and 24 nm, respectively, than those of R1.75_F2_8 at 2 mN and 34 nm. The small difference between pop-in length on P - h curves could be correlated to reduction of two sides of hexagonal pile-up (highlighted by red arrows).

The further change in topography is associated with imprints having longer pop-in displacement, and the corresponding load-displacement curves are shown in Figure 10 and residual impressions in Figure 15. In the majority of results, the pile-up pattern does not exhibit axial or hexagonal symmetry. It is also relatively higher and wider than in Figures 11, 12, 13, and 14, and is broken by a cross-valley. Its topography is qualitatively similar to that produced with 9.2 μm tip; however, the volume and area of the sink-in, which are visible on the profile in the valley direction, are relatively smaller. Moreover, the repeatability of the imprints is worse than that of 9.2 μm tip *i.e.*, similar P - h curves are associated with quite different pile-up/sink-in patterns, Figures 15(a), (b). For this reason, it is more difficult to confirm the tendencies observed in the evolution of

Table I. Parameter Values of Selected Imprints according to the Scheme in Fig. 7(a).

Name	Pop-in Load (mN)	P_m (mN)	H/L	Δ/P_m	l (μm)
R9_O17_13	9.73	10	0,018111455	0,027	12,4
R9_O17_6	10,23	20	0,057586207	0,4885	13,61
R9_O17_9	10,98	36	0,084047619	0,695	11,3
R9_O17_11	22,3	36	0,053947368	0,38	18,68

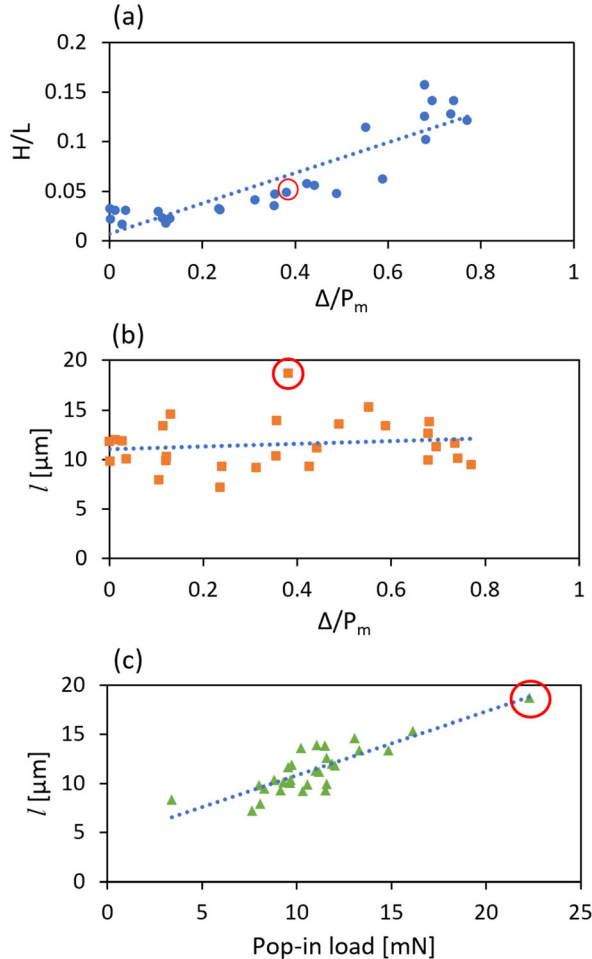


Fig. 8—Change of selected residual imprint parameters as a function of load increase after pop-in. (a) Correlation between normalized load increase after pop-in and the average ratio H/L , (b) correlation between normalized load increase after pop-in and total length l , (c) correlation between total length l and pop-in load.

imprints made with 2 μm tip with regard to pop-in load and maximum load. However, it can be seen that the relative depth of cross-valley is greater when the maximum load remains unchanged and the pop-in length increases, Figures 15(c), (d). The reduction of sink-in, when the difference between pop-in load and maximum load increases and the maximum load remains unchanged can be seen on the basis of profiles presented in Figures 15(a) and Figure 16. This tendency was also observed for 9 μm tip.

Furthermore, besides the cross-valleys, the long pop-in event could be linked to the irregular shape (discontinuities) at the bottom of the imprints that connect two sides of the valley, Figure 17, which is not found in indents with short pop-ins. This observation is in agreement with the results for the imprints of larger tip.

The evolution of pile-up for 1.75 μm tip indentation can be inferred based on the current evidence: in the first stage, a thin, wall-like circular pile-up is generated prior to the first pop-in c.f. Figure 11. Depending on the load at which the pop-in event occurs and the depth induced by such event, different scenarios could occur and change the shape of pile-up.

- Very short pop-in burst at low load would not introduce observable changes to the residual impression after unloading.
- Pop-in events at higher load that induce low depth change the pile-up formation to have a hexagonal shape with two-diminished sides, Figure 14.
- Imprints with high pop-in length in pile-up with cross-sectional valley.

a. Unloading pop-in A rare phenomenon was recorded during our experiment that a pop-in burst occurred during unloading process, Figure 10. To the best of the authors' knowledge, such occurrence has not been reported in nanoindentation tests for pure zinc. However, the existence of sudden change in unloading profile was reported for nanoindentation experiments for monocrystalline silicon as well.^[49–51] This change manifested in form of an instant decrease in depth and was termed elbow or “pop-out” during unloading process. It was attributed to the phase transformation from Si-II to a less dense Si-III and/or Si-XIII phases, hence, the sudden increase in volume.

In our tests, the unloading pop-in was observed more frequently for imprints made with 1.75 μm tip than for 9.2 μm tip. In addition, for the 9.2 μm tip, the unloading pop-ins occur at the loads close to the maximum load, while for the 1.75 μm tip, the pop-in on the unloading curve occurs at relatively lower load, even at 70 pct of the maximum load. For the majority of test with smaller tip radius, the pile-up pattern is similar to that observed for without pop-in, *i.e.*, axis-symmetrical or hexagonal ring, Figure 11. Only when a high load pop-in event occurs and causes a large displacement of depth (more than 130 nm), a cross-sectional valley is generated and the shape of pile-up pattern is closely resembled that produced by loading pop-in, Figure 13; however, the

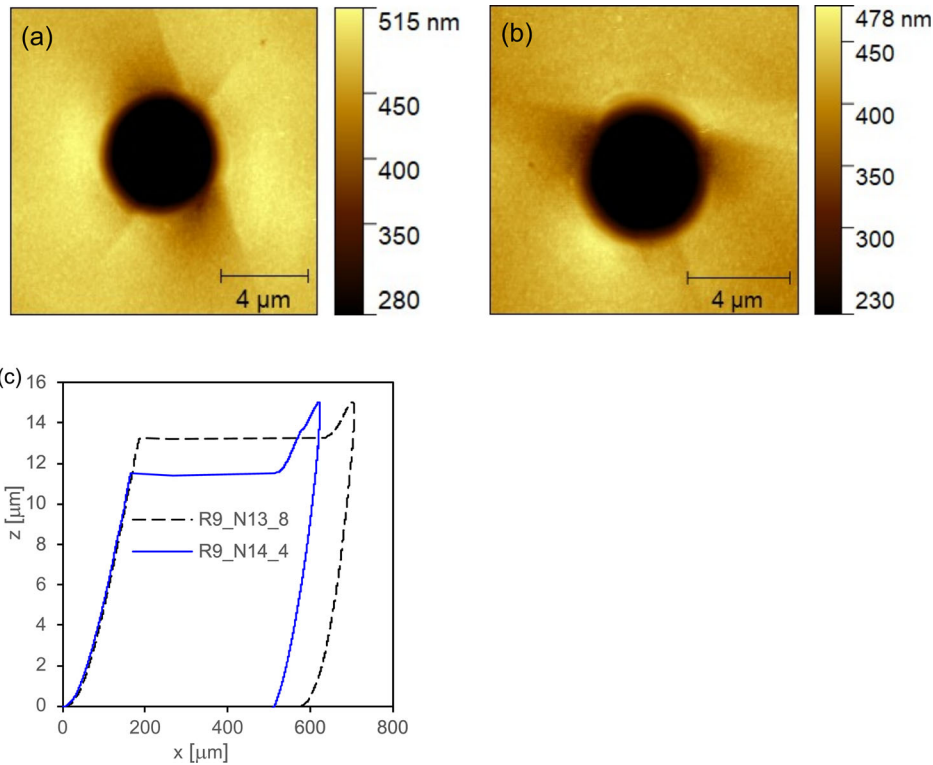


Fig. 9—Residual impression with double sink-in: (a) R9_N13_8, (b) R9_N14_4, and (c) load–displacement curves of aforementioned tests.

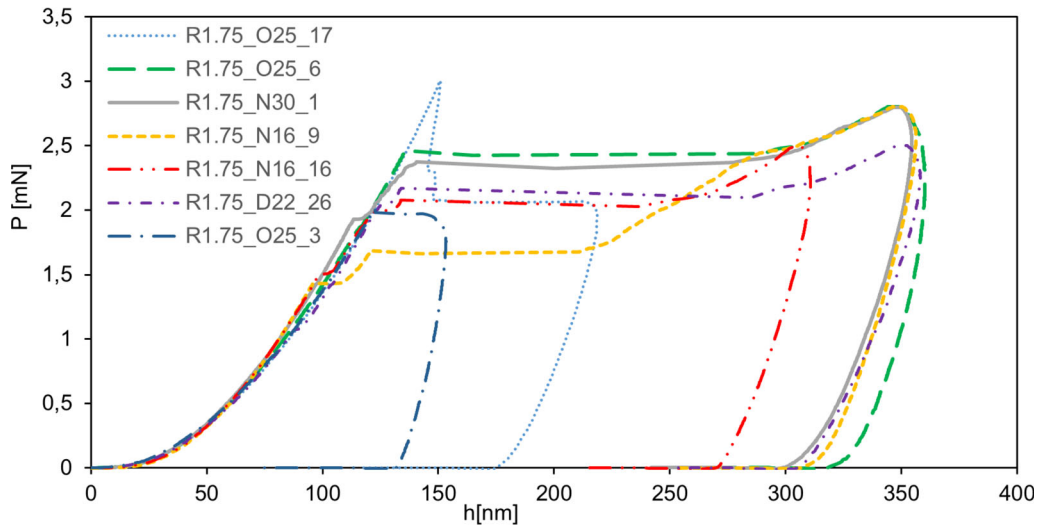


Fig. 10—Different types of load–displacement curves for analyzed indentation tests.

valley is less distinct. While there are rare cases of indents that have pop-ins events during both the loading and unloading processes, no result with more than one pop-in in unloading curve was recorded.

B. Pop-in Events Distribution

1. Results for 9.2 μm tip

In Figure 18, we presented a summary of results for the 9.2 μm tip indentation in terms of load *versus* length for the first major pop-in event during loading,

unloading, or holding process for tests with maximum load between 15 and 36 mN. The specific load levels and the number of indents are provided in Table II. The distributions of these two parameters are provided as well.

The distributions of these two parameters are provided as well. For pop-in load distribution, a notable peak can be seen from 8 to 9 mN, which contain the highest amount of result. The majority of results in this load range corresponds to a peak in pop-in length distribution (260 to 300 nm). It can be seen that,

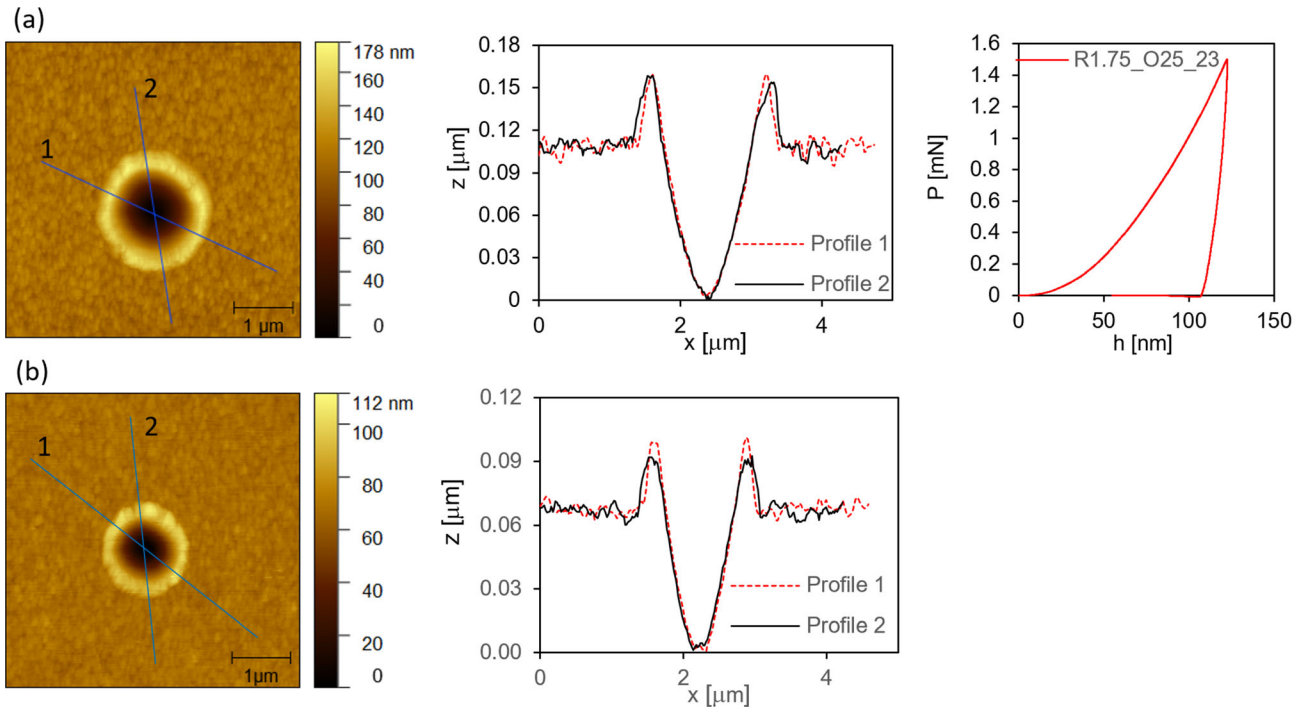


Fig. 11—Topography of residual impression for loads lower than pop-in load: (a) hexagonal pile-up and load penetration curve, (b) circular pile-up.

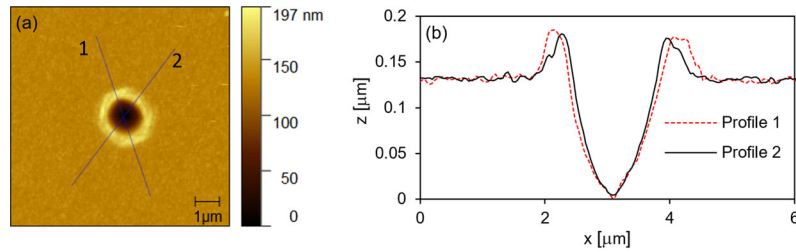


Fig. 12—AFM measure result of imprint R1.75_N29_3; (a) topography and (b) selected profile.

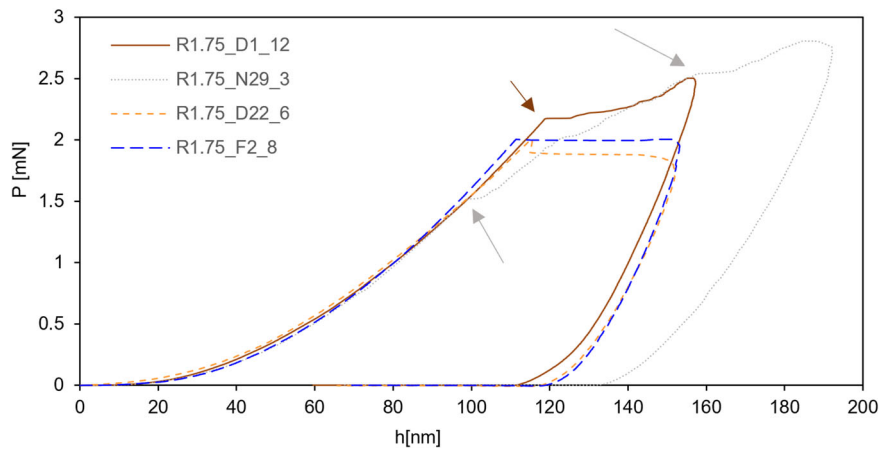


Fig. 13—Examples of load–displacement curves for imprints with circular/hexagonal pile-up (Color figure online).

while there is a scattering of pop-in parameters (regarding both the pop-in initiation load and the subsequent length) in our experiments, the majority of which are

concentrated in certain ranges, and that the pop-in induced load is quite repeatable. Moreover, a direct relationship between pop-in initiation load and pop-in

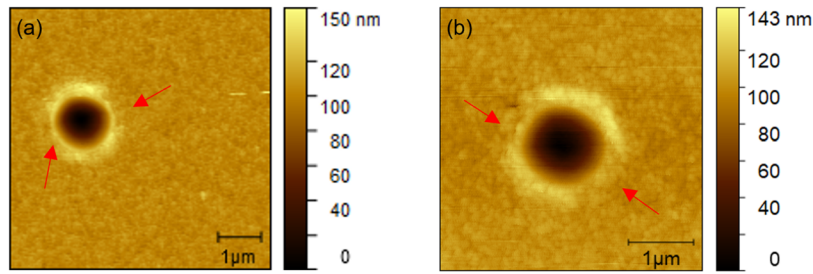


Fig. 14—Topography of residual impression for imprints with small pop-in induced depth. (a) R1.75_D22_6, (b) R1.75_F2_8 (Color figure online).

length can be observed, *i.e.*, pop-in events at higher load will induce respectively higher degree of displacement. One extreme outlier at the top right of Figure 18 is imprint R9_O17_11, which has been discussed in earlier section. Due to the higher concentration of pop-in events occurred at 8 to 10 mN, series of experiments were carried out for maximum loads of 10 mN and lower to examine the imprints shortly after or without pop-in events, and the results are not summarized in Figure 18 to avoid creating bias in our distribution.

The summary of data for the imprints are shown in Figure 19, which were examined with AFM for better understanding of their topography. The results are categorized based on their respective topography. The red point results represent the most commonly observed residual impressions, similar to that in Figure 3. In the middle region, there are two blue points indicating imprints with only pile-up formation on the surface, which have a large increase of load after pop-in event leading to the complete annihilation of sink-in as the residual impression expanded. On the bottom left side, there are the imprints that correspond to the smaller pop-in load group (4 to 6 mN) as demonstrated in Figure 18. Current evidence suggests that imprints in this group have neither pile-up nor sink-in (in other words, a flat surface around the imprint). An outlier can be seen in the bottom left corner of Figure 19 (highlighted with a red square), and this outlier is imprint R9_F10_11, which has been discussed in the earlier section to have the residual impression influenced by the second pop-in.

2. Results for 1.75 μm Tip

The distribution of pop-in load and length for 1.75 μm tip indentations is summarized in Figure 20. The black dots represent the imprints with pop-in during either loading and holding process, while yellow dots are for indents with pop-in during unloading. The specific load levels and the number of indents are provided in Table III.

Dissimilar to the distribution of pop-in induced load for larger tip indent, the results can be seen to form into two groups:

- The first group is composed of pop-in bursts with length lower than 40 nm, which skewed the distribution of pop-in length to the left (or bottom). This skewness is largely contributed by the pop-in events

of shorter length in a wide range of load level. 68 results were recorded in total for this group. More specifically, 42 results are for pop-ins during unloading (60 pct of total number of results for unloading pop-in), while the remaining 26 results are for pop-ins during loading and holding stage (24.73 pct of total number of results for loading and holding pop-in events).

- The second group consists primarily of pop-in events with length greater than 40 nm. The results in this group can be seen to show a direct proportion relationship between pop-in load and pop-in length, similar to that of experiments with the greater tip.

A large number of experiments at low load (1 mN and 1.5 mN) was done in this research to examine the indentation prior to pop-in, of which two (2) tests in 1 mN and twenty-five (25) tests in 1.5 mN load group were registered with pop-ins. In particular, the pop-ins for the smaller max load are during loading and induced less than 1 nm displacement, they are brief interruptions to otherwise smooth loading curves. For the larger maximum load, 21 out of 25 pop-in results occurred during unloading process. Some pop-in events of this group, while occurred at high load, *i.e.*, shortly after holding time produced very short depth (less than 10 nm); in other words, they contributed to the first branch of the distribution shown in Figure 20. Similar trend is observed for higher load at 1.8 and 2 mN with majority of pop-ins that are in unloading process, although less tests without pop-ins are recorded (the pop-ins events are more likely to happen as the maximum load increases). However, in the tests at higher max load (2.5 to 3 mN), pop-in excursions are present in all the tests, and very few tests with pop-in during unloading are registered. Even though the bursts displacement happened during unloading—the material is still considered under load as the spring back is still hindered by the indenter tip. This may be provisory explained by the hypothesis that unloading pop-in occurs due to prolonged stress under a certain critical load. Such hypothesis was formulated by Page *et al.*^[52] who found that pop-ins would eventually manifest

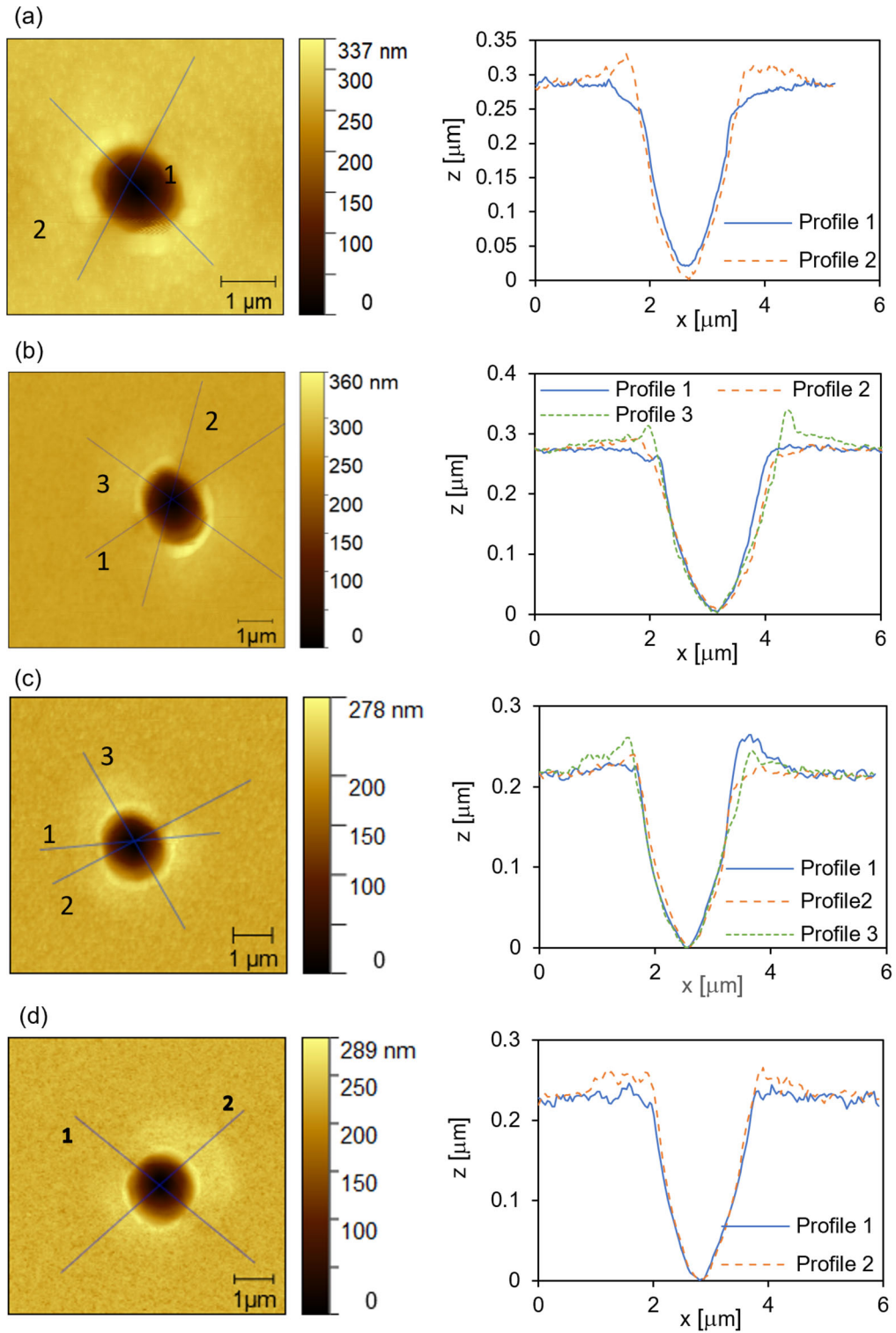


Fig. 15—Topography of residual impression and profiles for different ratios of pop-in load and maximum load, corresponding to load displacement curves presented in Fig. 10. (a) R1.75_O25_6, (b) R1.75_N30_1, (c) R1.75_N16_16, (d) R1.75_D22_26.

below a critical and repeatable pop-in load after a certain delay time, characteristic of a given sample conditions, and crystallographic orientation.

It should be noted that due to specific (two branches) distribution of pop-in parameters, it is difficult to establish a certain critical pop-in load, dissimilar to that of the distribution for larger tip imprints. The objective is, however, to better illustrate both types of pop-in

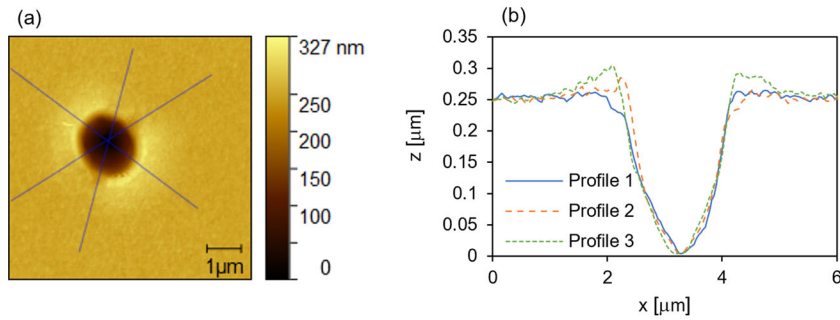


Fig. 16—Residual imprint R1.75_N16_9: (a) topography of residual impression for test with low pop-in load and high maximum load and (b) the selected profiles.

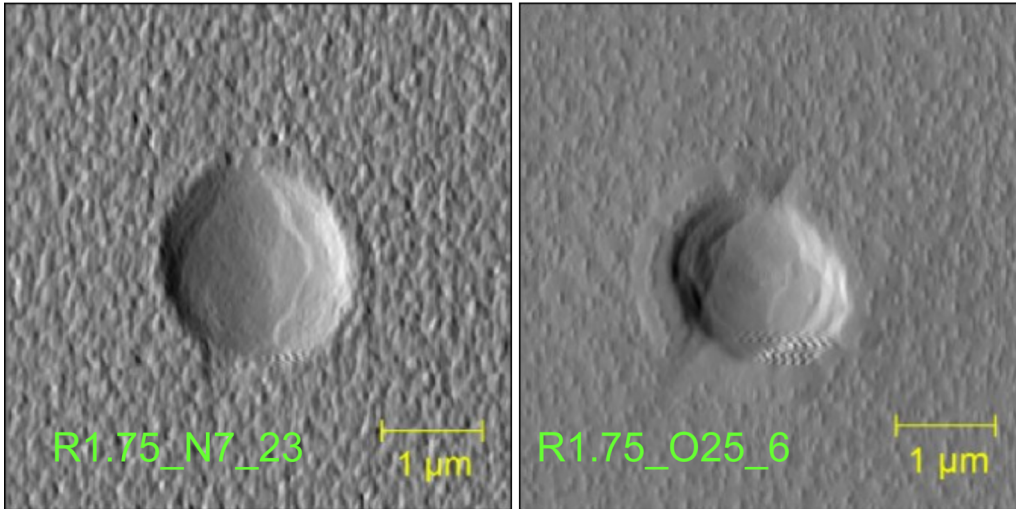


Fig. 17—Discontinuities in the bottom of the imprints corresponding to long pop-ins.

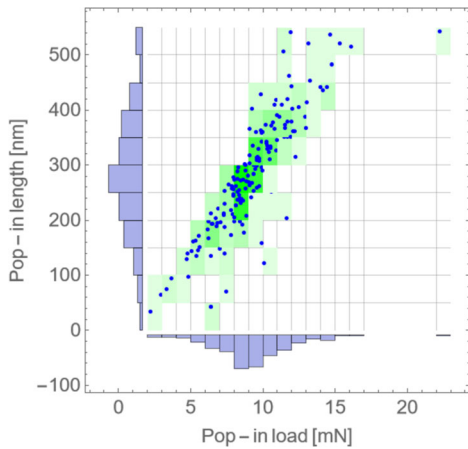


Fig. 18—Summary of pop-in load and pop-in length for $9.2 \mu\text{m}$ tip with respect to distribution of pop-in load and length for imprints with applied load within 15 to 36 mN. A peak in pop-in load distribution is observed at 8 to 9 mN.

behaviors, display similar trend of having two different branches of distribution as well as the probability of pop-ins to occur. Nevertheless, the observation that pop-ins occurring at higher load would induce a larger

displacement (the distribution of $R = 9.2 \mu\text{m}$ and second family of $R = 1.75 \mu\text{m}$ tip), as well as a reduced tip size coincides with a reduction in pop-in-induced load that has been previously reported by Cordill *et al.*^[53]

The summarization of the imprints measured with AFM is shown in Figure 21 for more precise studies of topography. The results are categorized and assigned different colors based on the pop-in burst location on $P-h$ curves as well as impression topography. The imprints with pop-in event on loading curve and with gaps in pile-up (black points) are located in the middle toward the top right side (high pop-in load and pop-in length). The results in this group show a positive correlation between pop-in load and length, which is similar to that of $9.2 \mu\text{m}$ tip radius imprints. The results with pop-in during unloading process are shown in blue colors and yellow for pile-up pattern with gap and without it, respectively. Blue point and a portion of yellow point results are seen to produce positive correlation between pop-in load and length, similar to that of loading pop-in indents. However, the pop-in load and pop-in length requirements to create an observable disruption in pile-up are higher for unloading pop-ins than that of loading ones. Tests with loading

Table II. Maximum Load Applied and the Number of Indents for Each Level for the $R = 9.2 \mu\text{m}$ Tip Experiment

Maximum Applied Load (mN)	Number of Imprints
15	45
20	10
36	35

pop-in do not exhibit the gap in pile-up, are colored green. A number of them occurred at high load and induced large displacement, these results are quite rare, and their residual impressions show circular pile-ups.

Pop-in events that induced low displacement (less than 60 nm) have a similar characteristic that is circular pile-up patterns with no gap, regardless of the pop-in load (both loading and unloading pop-ins). Imprints with hexagonal pile-up are marked with gray dots. This

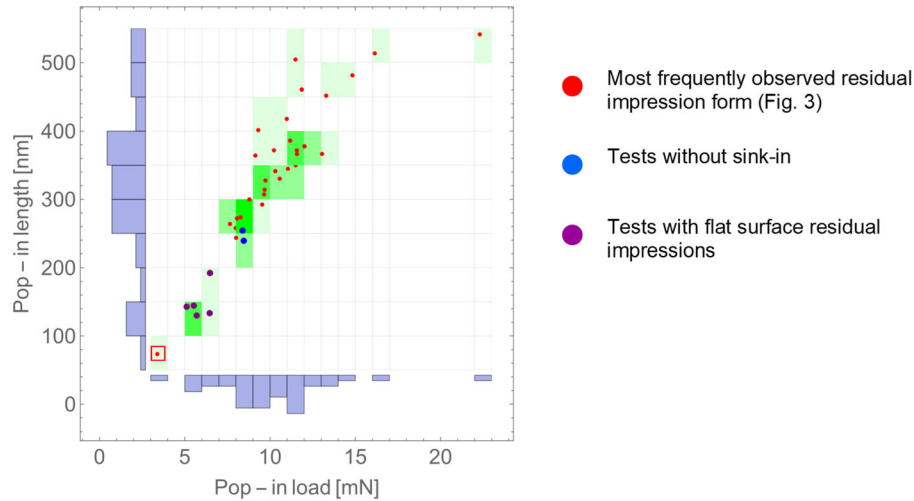


Fig. 19—Distribution of pop-in loads and lengths for tests with $9.2 \mu\text{m}$ tip and topography measured with AFM. The results are categorized based on their respective topography (Color figure online).

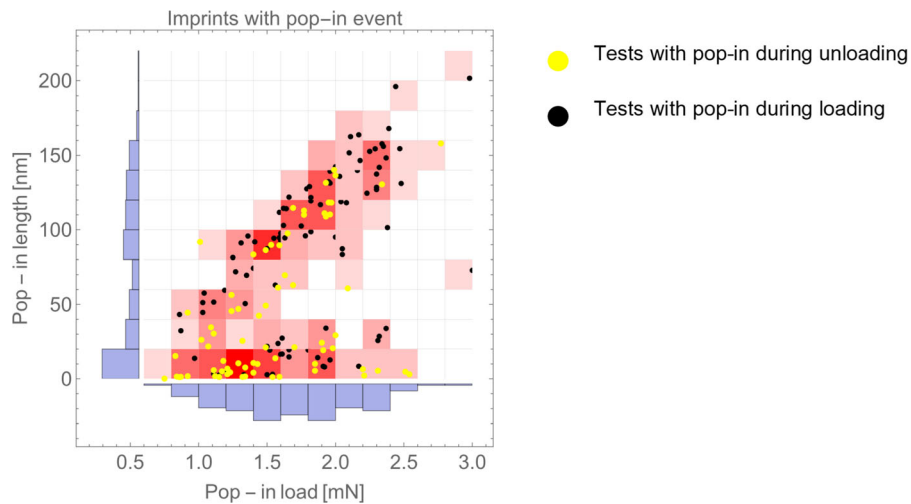


Fig. 20—Summary of results for $1.75 \mu\text{m}$ tip indentation, which shows two distinct families of distribution, with respect to distribution of pop-in load and length. The results are differentiated with regard to the type of pop-in events (Color figure online).

group includes both the loading and unloading pop-in imprints as their residual impressions show no noticeable distinctions between two types of pop-in. The results have not only medium to high (more than 1.5 mN) load, but also a particular pop-in length (between 15 and 40 nm), which is dissimilar to those with both low pop-in load and length at the bottom left and right corners of Figure 21. An outlier to this rule is highlighted by a purple square with very lower pop-in induced depth. That is indent R1.75_N29_3, and the explanation for such behavior has been provided in previous section.

C. EBSD Analysis

The residual impressions corresponding to different loads were examined using EBSD technique. The aim of this investigation was to correlate $P-h$ curve and surface topography of the residual impressions with orientation changes both inside the residual impression and on the free surface around the indents. The initial orientation of the examined sample surface was also captured. In the previous section, it was shown that the pop-in events

Table III. Maximum Load Applied and the Number of Indents for Each Level in the $R = 1.75 \mu\text{m}$ Tip Experiment

Maximum Applied Load (mN)	Number of Imprints
1	25
1.5	55
1.8	30
2	40
2.5	45
2.8	25
3	10

on $P-h$ curve are most commonly associated with the specific form of the residual impression, where pile-up is crossed by sink-in.

This typical impression is presented in Figure 22(a), with marked crystallographic directions. In Figure 22(b), the EBSD inverse pole figure map of such imprint in a direction parallel to the c -axis (indentation axis) is presented. The continuous change in misorientation on the pile-ups indicates that they were generated by slip. Taking into account their positions (on the directions $[2\bar{1}10]$ and $[\bar{1}120]$), we can conclude that the second-order pyramidal slip system $\{11\bar{2}2\} [\bar{1}123]$ was activated. The valley (sink-in) is generated in the direction $[\bar{1}2\bar{1}0]$, and this direction coincides with that of the main, large twin (bird wing) formed outside the residual impression, as shown in Figure 22(b).

The twin outside the imprint exhibits a misorientation of about of 86 deg with respect to the indented matrix basal plane, identified as $\{10\bar{1}2\} \langle 10\bar{1}\bar{1} \rangle$ twin.^[41] Due to c/a axial ratio of zinc (1.867), this is a compression twin,^[54] causing contraction along the c -axis, which manifests as a sink-in. The presence of twins due to indentation on the basal plane has been reported by Yoo and Wei^[55] as well as Nayyeri *et al.*^[18,41] for magnesium.

The twins were located inside the residual impression in the form of small cells, surrounded by other cells that exhibit orientations closer to the matrix's orientation. This can be interpreted as the formation of sub-grains under the indent. The presence of sub-grains in residual impressions made in Mg was previously reported by Nayyeri *et al.*^[18]

Multiple FIB milling was used to further examine twin activity beneath the bottom of the imprint. Traces of twins in the form of small cells were consistently found at approximately the same location, extending to a depth of up to 840 nm, demonstrating that the twins extended significantly below the surface, as shown in Figure 23.

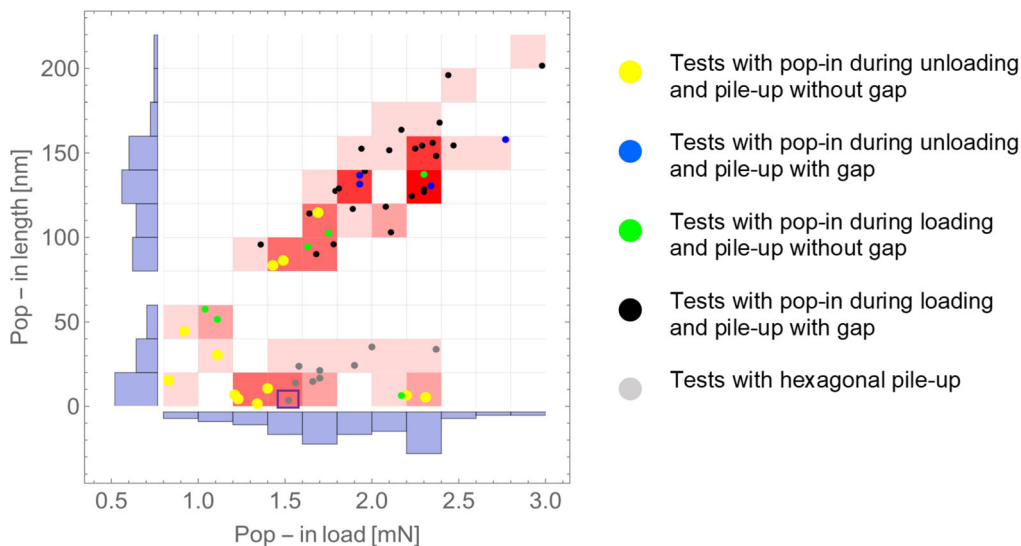


Fig. 21—Distribution of pop-in loads and lengths for tests with $1.75 \mu\text{m}$ tip and topography measured with AFM. The results are categorized based on their respective topography and the type of pop-in events (Color figure online).

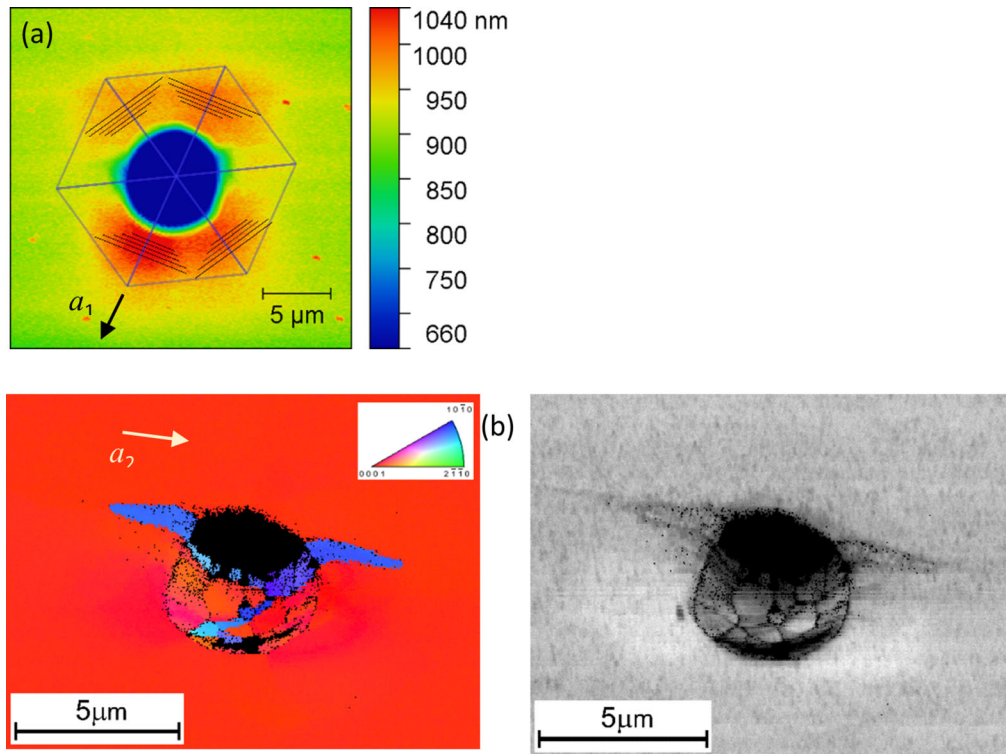


Fig. 22—Residual impression for 9.2 μm tip: (a) pile-up/sink-in pattern, measured with AFM, with marked crystallographic directions, (b) misorientation and image quality maps from EBSD.

The EBSD analysis was also performed for imprints corresponding to different types of material responses (Section III–A–1). Figure 24 shows the P – h curves for the impressions, and the EBSD results of which are shown in Figures 25, 26, 27, 28, 29, and 30. For each imprint, we show the misorientation map, the image quality map (IQ), and the surface gradient map obtained by AFM (derivative of the Z -value with respect to the X -axis, referred to as the “gradient map”). It can be seen that a part of the surface inside each imprint is not properly indexed, and this is caused by shadowing of this part by pile-up and/or indenter contact boundary. It should be noted that, although the orientation of individual regions has been correctly identified, a straight line on the AFM map corresponds to a curved line on the EBSD map due to the inaccurate back transformation of the impression cavity after EBSD measurement. Therefore, the shape of cells on the EBSD map is not exactly (does not correspond to) the same cells as on the gradient maps. For the EBSD results, multiple cells are visible, with orientations similar to those presented in Figures 22 and 23 (around 86 deg and less than 13 deg). A closer comparison of the IQ maps and the gradient maps shows that on the latter, the cellular structures can also be detected, *i.e.*, the bottom of the imprint is not perfectly smooth, and there are small steps between cells. These steps are a result of different elastic recovery during unloading, as the cells have different elastic moduli due to different orientations (50 GPa along c -axis and 108 GPa in the

perpendicular direction). This effect is more evident at greater maximum load.

For test R9_J21_18, where maximum force (6 mN) was set to be lower than the pop-in initiating force, the residual impression can be seen to be relatively smooth in the AFM measurement, Figure 25. EBSD map shows no appreciable distinction in terms of orientation from the background. The indentation had the effect to flatten the roughness as expected; however, no irregularities or sub-grains could be found in this case. This is indication that the plastic deformation prior to pop-in events proceeds purely by slip on a single slip plane.

In test R9_J21_15, the loading process ended shortly after pop-in event; the pop-in initiation load is 9.35 mN, Figure 24, which is within a more populated load distribution as shown in earlier section. In addition to larger penetration depth, a cross-valley sink-in topography was detected with AFM technique, Figure 26(a). Twinned material can be found both within the valley and in the direction of the valley within the residual impression, although not to the entire length of the valley. A smaller trace of twinning was detected within the residual impression on the left side as well. Twinning is not the sole deformation mechanism, in the observable area within the residual impressions; cells with smaller misorientation with respect to initial orientation [0001] can be seen, thus, providing the notion that more than one slip systems were activated in order to accommodate the enormous displacement. In comparison to test R9_J21_18, it can be concluded that the

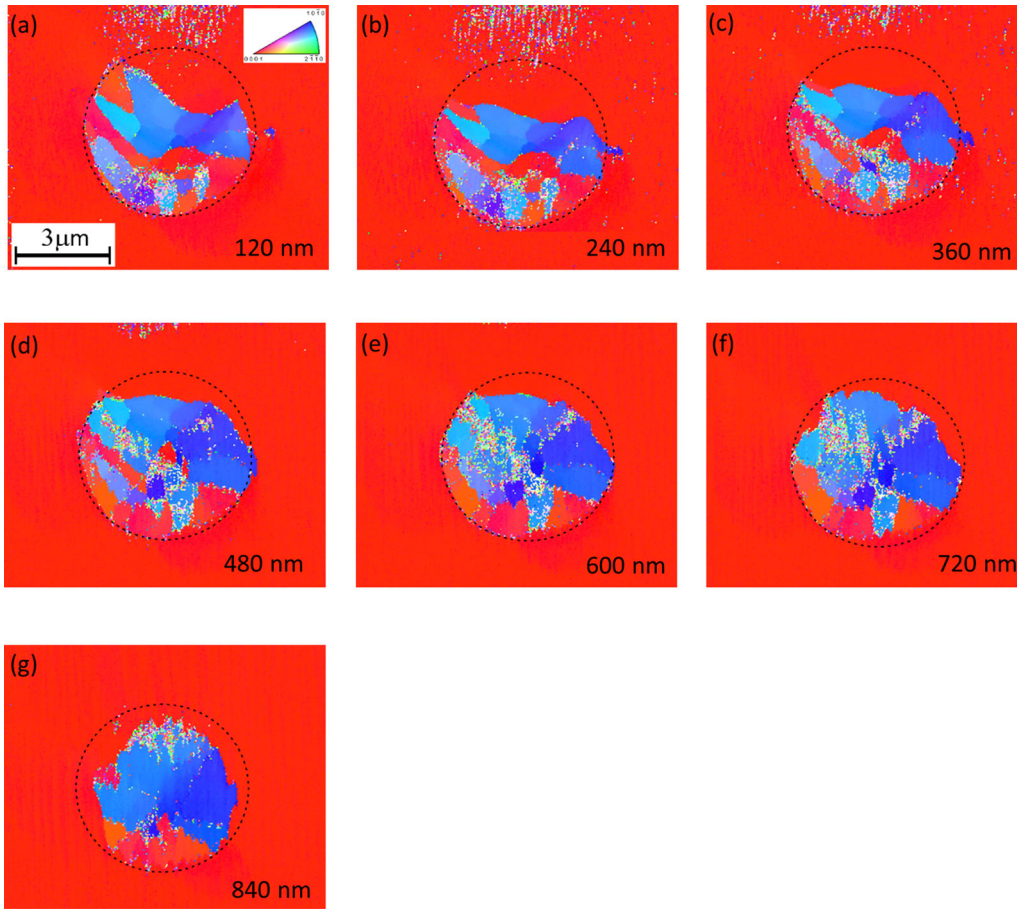


Fig. 23—Misorientation at different depths below the free surface for typical impression after long pop-in and pop-in initiating load close to the maximum load (similar to the R9_O17_13, Fig. 5) (a) through (g).

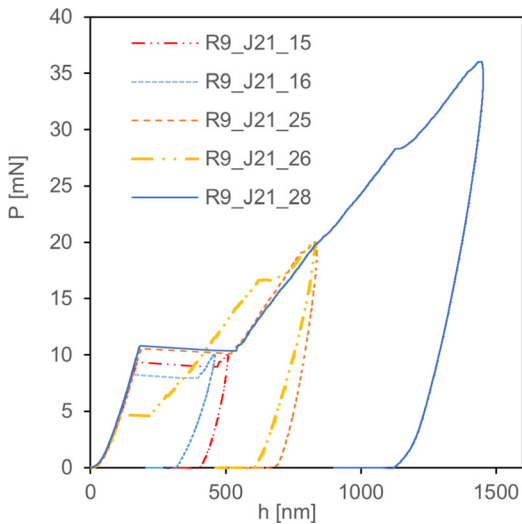


Fig. 24—Load–displacement diagrams for residual impressions analyzed with EBSD and scanned with AFM. The selected tests correspond to the typical material responses presented in Section III–B–2: different load increases after pop-in event.

twins (those inside the imprint as well as “bird wings”) and wide pile-ups were created simultaneously during the pop-in burst.

The pop-in displacement also plays an important role here as shown in Figure 26(b) of indent R9_J21_16. The slightly shorter pop-in length (and lower pop-in initiating load) resulted in a very thin strip of twinned region, deformation by slip is observed to be the dominant mechanism here. For test R9_J21_26, the first pop-in load is even lower than that of indent R9_J21_16 at 4.71 mN, and in spite of the second pop-in at higher load, there is a lack of twin on the surface layer, Figure 27. In both cases, the cross-valley could have been created, but as we have discussed in the previous section, the length of the valley is proportional to the pop-in length and does not change with the increment of load after pop-in. Thus, it is reasonable to assume that the cross sink-in for such short pop-in event, if it existed, should be minuscule and “swallowed” by the indent as contact area increases. Of more noteworthy, the residual impression of indent R9_J21_26 is divided into several smaller regions and was confirmed by EBSD mapping to have cells with a small degree of misorientation. This indicates that the drastic change in orientation of matrix, *i.e.*, twinning is not necessary for material to accommodate smaller displacement burst; hence, deformation by slip is preferable, which resulted in the creation of microscale grain structure-like within the residual impression.

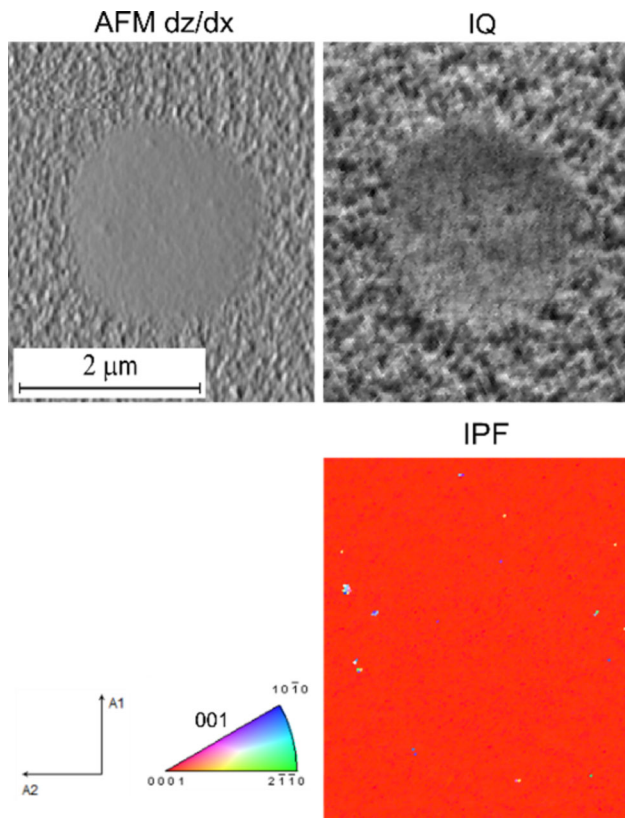


Fig. 25—Maps for the residual impression R9_J21_18 obtained from AFM and EBSD measurements: surface gradient map, image quality map, and misorientation map.

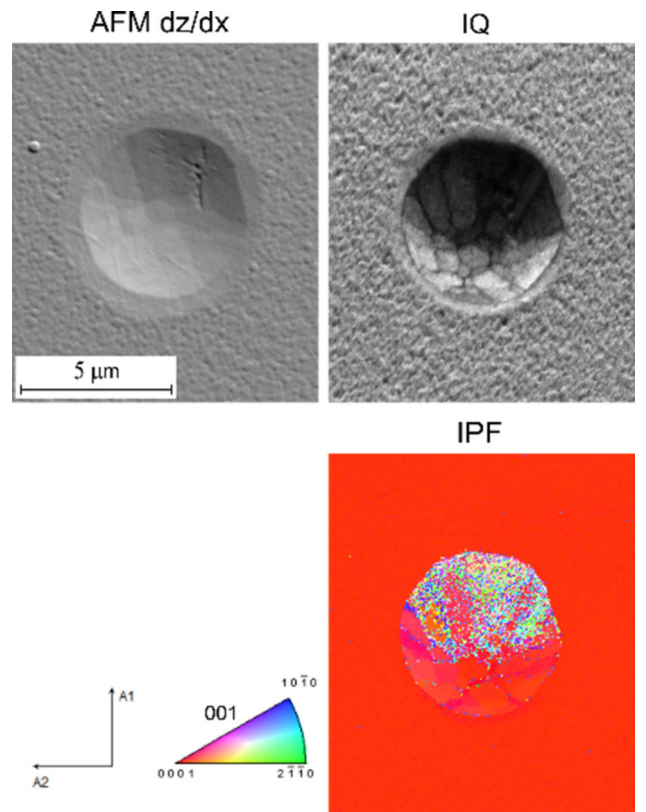


Fig. 27—Maps for the residual impression R9_J21_26 obtained from AFM and EBSD measurements: surface gradient map, image quality map, and misorientation map.

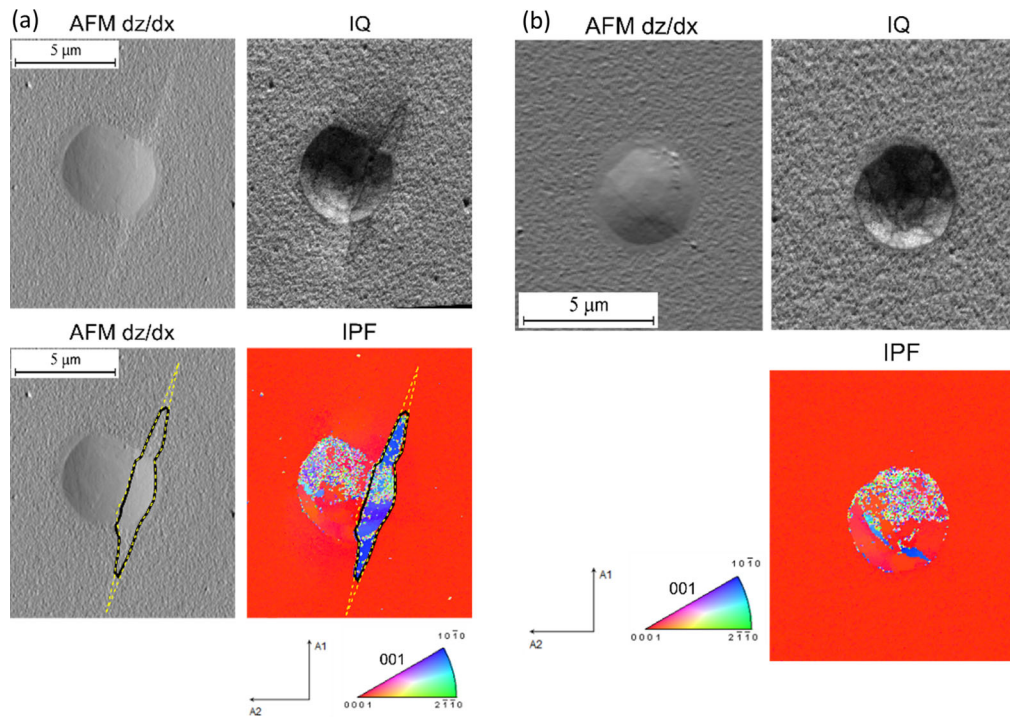


Fig. 26—Maps for the residual impressions obtained from AFM and EBSD measurements: surface gradient map, image quality map, and misorientation map. (a) R9_J21_15, (b) R9_J21_16.

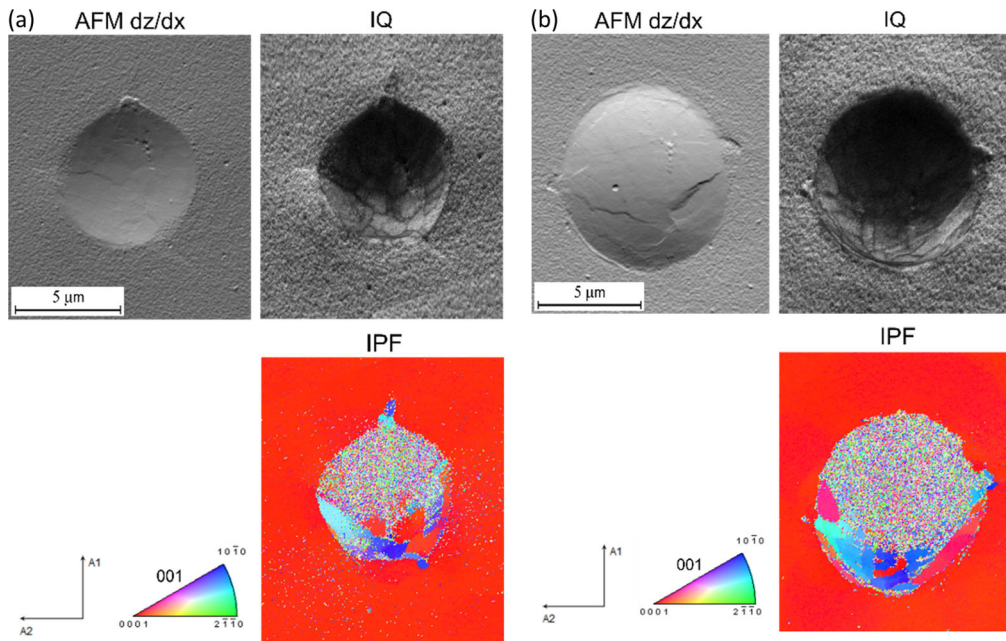


Fig. 28—Maps for the residual impressions obtained from AFM and EBSD measurements: surface gradient map, image quality map, and misorientation map, (a) R9_J21_25, (b) R9_J21_28.

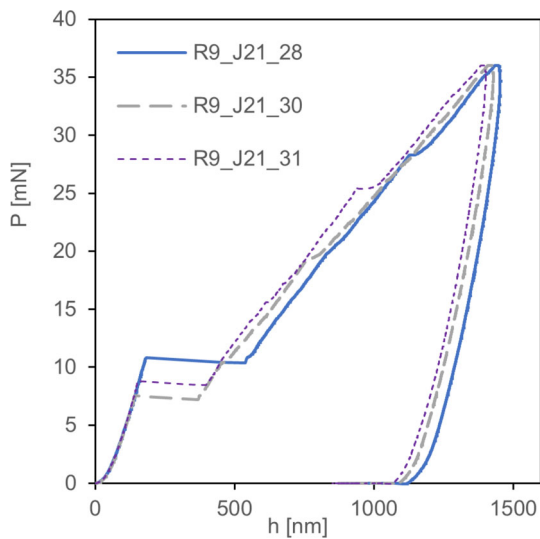


Fig. 29—Load-displacement diagrams for residual impressions analyzed with EBSD and scanned with AFM: different pop-in initiation loads and the same maximum load.

For the imprint R9_J21_25, which has the similar maximum load as R9_J21_26 at 20 mN (refer to Figure 24), with pop-in event occurred at higher load (10.58 mN), a miniscule sink-in depth was detected, Figure 28(a). EBSD map provided the evidence that similarly to imprint R9_J21_15, this small sink-in also contains a twinned region. However, dissimilar to the imprint R9_J21_15 with a smaller maximum load, twinned material is not only concentrated to the cross-valley, but it is swallowed by the increasing impression.

For imprints at maximum load of 36 mN, the $P-h$ curves of the selected experiments are shown in Figure 29, and the higher misorientation values than that of lower load imprints were observed. The portion deformed by slip shows multiple cells of different orientations, Figures 28(b) and 30 not unlike that observed in test R9_J21_26. Furthermore, in all examples, the twin areas are not homogeneous but rather fragmented into a cell-like structure, small amount of slip deformation can be seen within the twin formation. For indent R9_J21_28, Figure 28(b), which has high pop-in initiation load at 10.83 mN, twinning outside of the residual impression can be seen inside the small-wing-shaped regions. At lower pop-in initiation loads, for example, indent R9_J21_30 and R9_J21_31 at 7.54 mN and 8.81 mN, respectively, the sink-in is not clearly observed after such large increase of load; thus, the twin is confined to the residual impressions, Figures 30(a) and (b).

An interesting correlation can be seen between the profiles obtained from the imprint topography maps and the misorientation profiles from EBSD maps. The more detailed analysis of the EBSD results: image quality (IQ) map, Kernel Average Misorientation (KAM) map, and misorientation profiles over the selected sub-grains show the misorientation variation with respect to the starting point (matrix) and the “point-to-point” variation is shown in Figures 31(a) and (b) for the imprints R9_J21_26 and R9_J21_31, respectively. On the IQ maps, the crystallographic orientation of cells is schematically marked.

For indent R9_J21_26, the misorientation between cells is relatively low (red lines). The two peaks on the red lines in both figures are the “boundary” of the starting cell, and when the profile leaves the residual

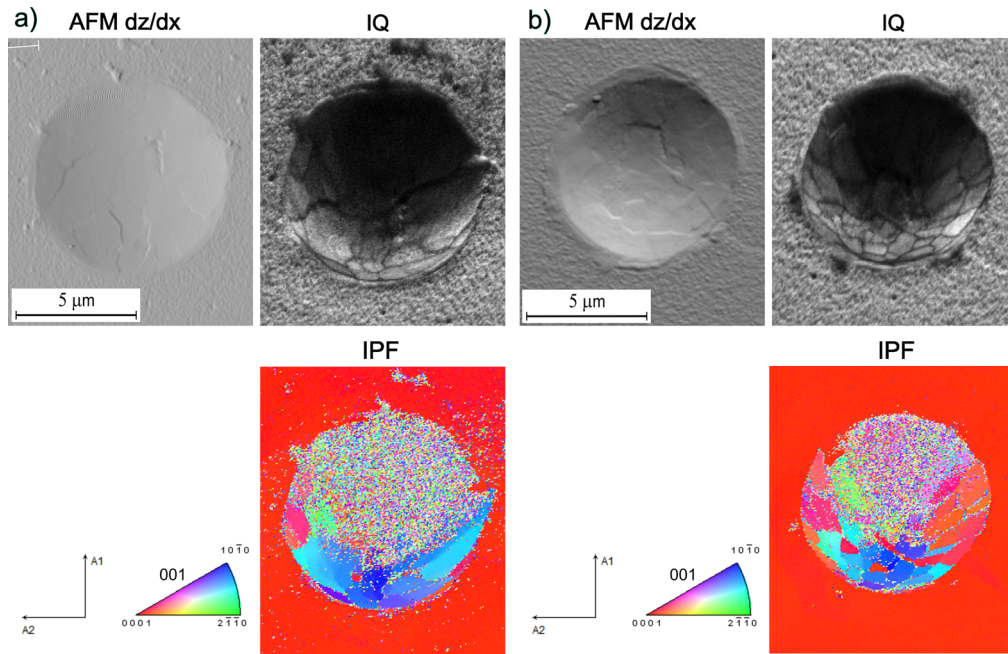


Fig. 30—Maps for the residual impressions obtained from AFM and EBSD measurements: surface gradient map, image quality map, and misorientation map. (a) R9_J21_30, (b) R9_J21_31.

impression,, it returns to the surface close to the basal plane. In the imprint R9_J21_31, the profiles over cells that are deformed by slip and by twinning, are shown as profile 1 and 2 in Figure 31(b), respectively. In profile 1 there is relatively little point-to-point misorientation, similar to indentation R9_J21_26. However, there is only one large peak in this profile, corresponding to the normal, undeformed surface. While for profile 1 the change in orientation from point to point is rather small for cells formed by dislocation interaction, there is a continuous change in misorientation that accumulates to about 10 to 15 deg. For twinned cells, as shown in the previous section, the misorientation is about 86 deg. The drop in the middle of the blue profile is due to a cell that has been deformed by slip, as shown in the IPF map.

For the same tests R9_J21_26 and R9_J21_31, the profiles with a similar position were also extracted from the topography maps (AFM) and is shown in Figure 32, to illustrate in more detail the steps observed on the gradient maps above. For the topographic profiles, the spherical shape of the impression has been removed to better show the small unevenness inside. The profile corresponding to the twin cells (profile 2 of test R9_J21_31) exhibits greater waviness in comparison to the profiles with cells generated by slip, for example, profile 1 of R9_J21_31 and both profiles of R9_J21_26. This indicates that the difference in height between neighboring cells is greater when they are produced by twinning. This qualitatively agrees with greater misorientation values observed on profiles for the imprint with twins. Thus, the height of steps between the adjacent cells increases when the difference in their misorientation increases. This is an effect of local difference in the elastic spring back after indentation test, since the

differently oriented sub-grains have different elastic stiffness in the indentation direction

1. Evolution of microstructure: detwinning

An additional significant finding in our research is the possibility of detwinning both within the valley and inside the indent. The trace of the twin can be observed within several days following indentation. However, after one week without any alterations or tampering to the surface, given that the samples were preserved in a desiccator between experiments, there is an absence of detectable twins in the previously confirmed twinned region.

The phenomenon of detwinning was discussed by Nayyeri *et al.* in^[41] as discontinuities in unloading curves, indicating that it occurs during the unloading process, which could result in the absence of detectable twins after the experiment. However, in our experiments, no such discontinuities were observed in the unloading curves. As noted above, twinning can still be detected after unloading, with a reduction in twins occurring only after a certain amount of time has passed. Future research should focus on this aspect of the material.

D. Size Effect: Comparison of Deformation Modes for Indentation with Different Tip Radii

The normalized $P-h$ curves for $9.2 \mu\text{m}$ tip and $1.75 \mu\text{m}$ tip are compared in Figure 33. For both tips, the maximum load corresponds to the maximum value that can be achieved without triggering the pop-in burst. Following observations can be made.

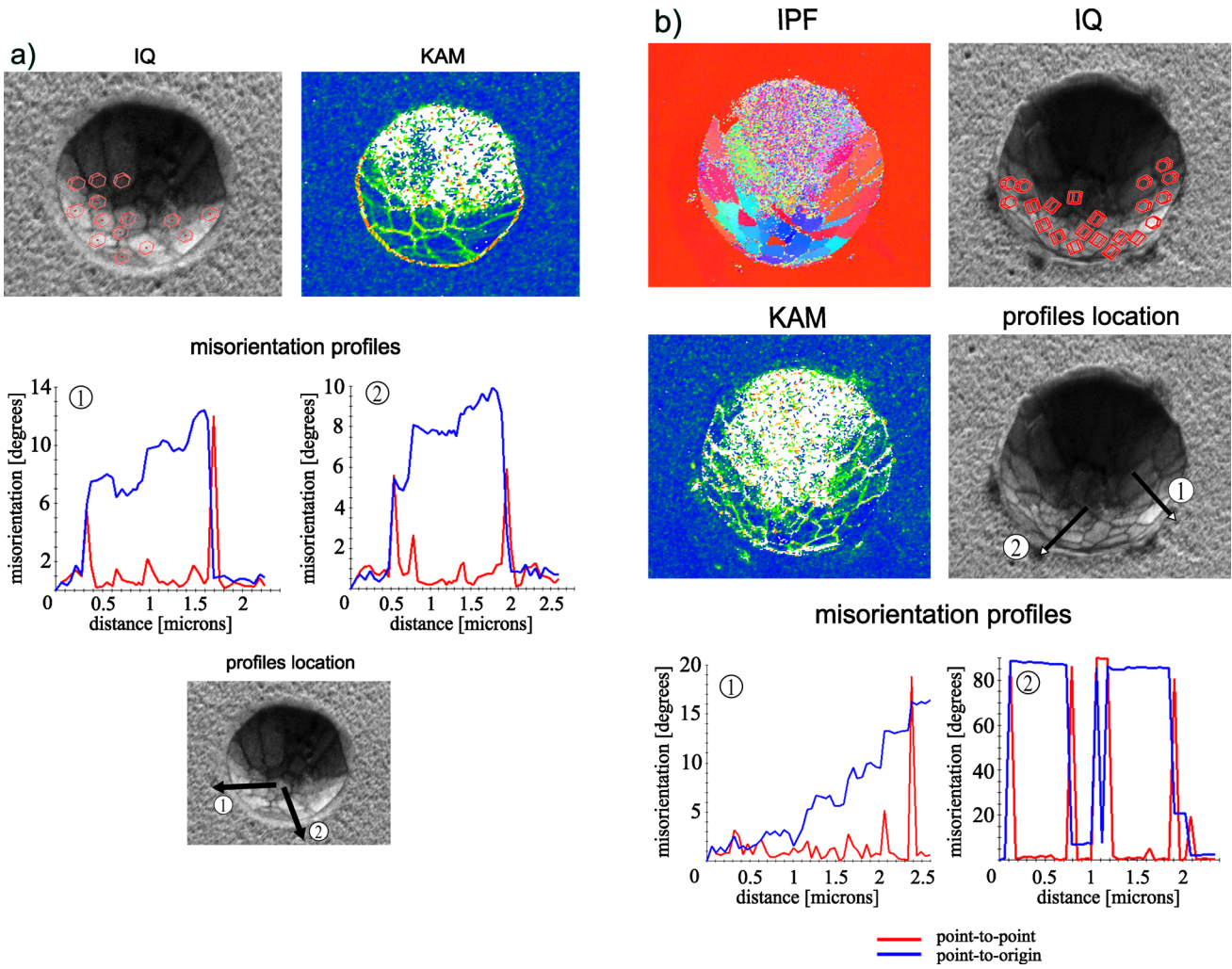


Fig. 31—More detailed analysis of EBSD results for imprints R9_J21_26 (a) and R9_J21_31 (b): image quality map with marked orientation of selected cells, Kernel Average Misorientation map, and misorientation profiles over the selected cells (Color figure online).

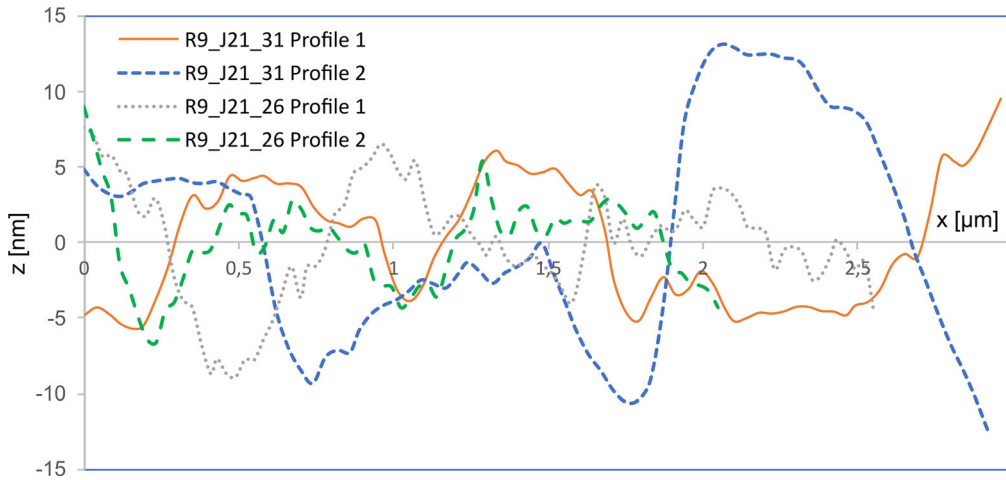


Fig. 32—Unevenness in residual impression after removal of spherical shape for indent R9_J21_31 and R9_J21_26.

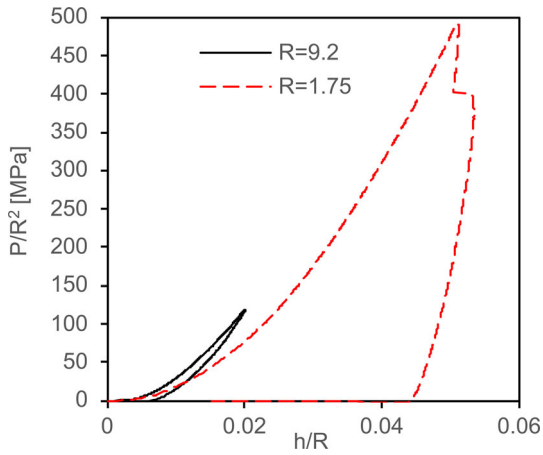


Fig. 33—Load–displacement curves for two tips.

i.

For the indentation with $1.75 \mu\text{m}$ tip, the pop-in (and consequently twinning) starts at much higher P/R^2 ratio, than for $9.2 \mu\text{m}$ tip.

ii.

The $9.2 \mu\text{m}$ tip curve exhibits greater hardening than that corresponding to $1.75 \mu\text{m}$ tip.

iii.

The relative depth of the residual impression, h/R , is much greater for $1.75 \mu\text{m}$ tip

The first observation (i) confirms a general rule for materials, in which the deformation prior to pop-in is purely elastic that in the normalized coordinates, the load corresponding to pop-in load (which is usually associated with start of plastic deformation) for $1.75 \mu\text{m}$ tip is higher than that for $9.2 \mu\text{m}$ tip. For such materials, the contact pressure can be calculated using Hertz formulas, and this leads to the conclusion that pop-in occurs at higher contact pressure for smaller tips. This is explained by a smaller high stress zone beneath smaller tip, and consequently smaller amount of affected pre-existing dislocations that can activate plastic slip (indentation size effect). However, in zinc, we have other mechanism, and plastic deformation starts as the slip on certain planes at the beginning of loading. The pop-in burst begins at the moment that plastic slippage has already exited, and creates a plastic deformation, presumably twinning, on other planes. Advanced numerical simulation is required to calculate stress state at the start of pop-in.

The second observation (ii) does not agree with tendency observed for many metals, where prior to the pop-in the hardening, estimated on the basis of normalized $P-h$ curves that correspond to elastic deformation and, thus, coincide for all tip radii. For both tips, we observe plastic deformation, and we have inverse size effect, *i.e.*, greater hardening for the greater tip while according to the usual explanation of size effect, indentation with smaller tip is associated with higher hardening, because the tip generates greater strain gradients. It should be noted that this inverse size effect manifests in the plastic deformation prior to pop-in.

The third observation shows that the plastic deformation mechanisms responsible for the prior to pop-in plasticity may accommodate much higher strains for smaller tip than for greater tip.

IV. DISCUSSION

A. Deformation Mechanisms

In the first stage of the indentation test, below the critical pop-in initiating load, the material deforms plastically by slip, as evidenced by the mismatch between the loading and unloading curves and the deviation from the Hertz elastic relationship. The depth of penetration at this stage is much greater than the average height of the surface asperities, thus, eliminating the possibility that the indentation merely flattens them during loading. The lattice orientation under the indenter does not change significantly, Figure 25. The residual impression is noticeably smooth, without surface irregularities and pile-up pattern. This indicates the plastic deformation is realized by slip on the basal plane which exhibits the smallest RSS,^[2] and is parallel to the sample surface; therefore, the pile-up is not produced at small deformation. Plastic deformation probably starts in small spots corresponding to flattened asperities, but eventually a small plastic zone is created below the indenter in bulk material. The shape (slope) of the $P-h$ curve at this stage does not depend on the specimen annealing, but the length of this stage (maximum force that initiates pop-in) does. This suggests that the density of pre-existing dislocations does not affect the basal slip but changes the starting point of subsequent mechanisms of plastic deformation.

As the indentation progresses, the plastic zone increases and reaches a certain limit where the basal slip, which is perpendicular to the direction of indentation, will not accommodate further displacement of the indenter. A further increase in penetration depth, *i.e.*, pop-in displacement, is associated with the generation of a pile-up which can be produced by activation of dislocations on the pyramidal and/or prismatic plane. The shape of the $P-h$ curves indicates that activation of these systems requires a certain level of stress. The associated pop-in event is explained as an effect of dislocation avalanches, which start when a sufficiently large stress is applied to an even small region (zone) with a local high density of pre-existing dislocations. The distribution of such zones depends on the annealing process, and this is confirmed by our experiments: the pop-in initiating load depends on this process. On the other hand, pop-in event has a random character since the zones with higher dislocations density may be randomly distributed after annealing. The duration of pop-in event is very short, so we cannot observe the evolution of plasticity during pop-in, but in the previous sections, we have carefully analyzed the state after pop-in using EBSD and AFM. In general, inside of the contact boundary, we observed cells having different misorientations. They can be classified into two groups: the first that are generated by dislocation interaction,

called as “slip sub-grains,” have a misorientation of no more than 14 deg, and the second, called “twin cells,” have a misorientation of about 86 deg that corresponds to compression twins in zinc, Figures 25, 26, 27, 28, 29, 30, and 31. The latter may appear also outside the contact boundary, if the pop-in length is sufficiently large.

The size and number of sub-grains produced may be different for different indentations, even though the material response in term of the $P-h$ curve is very similar. On the measured $P-h$ curves, the pop-in part is approximated only by 2 to 3 points, as the process is very fast. These points indicate that the load during pop-in slightly decreases and the displacement considerably increases. In fact, the pop-in process is more complex and the load may oscillate when the pop-in displacement increases during the process, and this may be associated with generation of the sub-grains. The load fluctuations are not shown on the $P-h$ curve due to following reasons: the process is controlled by the load, so the system does not allow the load to drop significantly and the points where the load may fall are not registered due to the limited registration frequency (100 Hz). While the stress state can be estimated using crystal plasticity theory in the initial, pre-pop-in phase, it becomes much more complex during and after the pop-in event as the structure of the material changes locally and instead of a single crystal, a polycrystal is formed under the indenter. The generated cells are an effect of slip and twin plasticity. The high velocity of the pop-in event does not allow to detect which slip system is activated as a first after the initial phase. On the surface around the imprints, however, there are no cells, so the pile-up growing simultaneously with the cells is produced by slip. Its shape indicates that second-order pyramidal slip was most active. The character of sub-grains can be correlated with the length of pop-in; for the longest pop-in, we observed long twins in form of “bird wings” outside of the residual impression, while for short pop-in, only slip sub-grains are produced.

It should be noted that when twinning plasticity occurs, the large pop-in displacement may also result from a change of orientation in a certain volume of material under the indenter. If twin is created in the examined single crystal, the c -axis rotates by 86 deg and after twinning, the a -axis instead of the c -axis has a vertical direction in the volume of twin cell. Thus, the vertical dimension of this volume diminishes. This diminishing dimension is manifested in two ways: on the $P-h$ curve as an additional displacement on the pop-in burst since twins are generated in a very short time and on the topography of residual impression in a form of sink-in (cross-sectional valley outside of the contact boundary, between pile-ups)

If the load increases after the pop-in event, the deformation is quasi-static in nature, and when the new pop-in occurs (if at all), its length is much smaller. In this phase, the deformation mechanisms are depended on the state of material at the point when the first pop-in displacement is finished. At this point, two types of microstructure are observed, *i.e.*, only the slip sub-grains are present or both slip and twin cells can occur. These

two types of material structure are maintained as the load continues to increase, the only difference being the dimensions of the new cells produced and the fragmentation of the existing cells. If twins are not produced on the first pop-in, they usually are not on subsequent load increases. The large “bird’s wing” twin that occurs outside the imprint after the first pop-in will not grow as loading continues, but will be swallowed by the growing imprint. Thus, during and after the pop-in event, we have similar mechanisms of deformation, the sub-grains grow and/or multiply, and in differently oriented grains, different slip/twin systems can be activated.

V. CONCLUSIONS

In this work, the nanoindentation behavior of c -axis-oriented Zinc single crystal was investigated using tips of different radii on samples with minimal near-surface defects, as evidenced by the observation of substantial pop-in events. The residual impressions exhibited complex shape that was a superposition of axis-symmetrical/hexagonal pile-up and cross-sectional valley (sink-in). This is a result of simultaneously occurring deformation mechanisms: slip and twinning. The impressions were influenced by the characteristics of the pop-in bursts. For such reason, the results were categorized based on their respective pop-in load and length.

The deviation of the unloading data from the loading one prior to the first pop-in event is associated with slip plasticity. The subsequent large pop-in is primarily linked to the contraction twins, but the slip plasticity is also activated at the same time. The latter manifests as a pile-up which is broken by a valley (sink-in) resulting from twinning. The length of the valley depends on the intensity of pop-in and does not expand further if the loading continues after the pop-in but the valley is rather “engulfed” by an expansion of the imprint. The twins occur inside the imprint in the form of sub-grains and outside the imprint, in the valley, in the form of a “bird wing.” Contrary to the results reported in the literature, this form of the residual imprint is observed in our experiments when indenting on the basal plane. The change in the pile-up/sink-in form with the increase in the pop-in was shown for the results corresponding to 9.2 μm tip. For the 1.75 μm tip, the observed trends are less obvious. The sink-in pattern also is more distinct for the greater tip indents than for the smaller tip.

In spite of low density of pre-existing dislocation (after annealing), a purely elastic response of the material was not noticed, but three stages of deformation mechanisms can be distinguished. In the initial phase of indentation, the elastic-plastic deformation is observed, but it is limited to the slip on the basal plane. Once the pop-in burst starts, slip on other planes and twinning are activated, and then, during pop-in burst, they develop simultaneously. In the third stage, when loading increases after the pop-in, both mechanisms are continued.

While there are some qualitative similarities between residual impressions produced by greater and smaller tip, we have quantitative difference in the load–penetration curves when presented in normalized coordinates. Comparing the curves reveals an inverse size effect before the pop-in event and normal size effect after the pop-in event.

This result, as well as other interesting observations like pop-in burst during unloading process, or detwinning that occurs over time without applying additional load or heat, requires farther investigation.

ACKNOWLEDGMENT

The research leading to these results received partial funding from the National Science Centre in Poland under Grant No. 2018/31/B/ST8/03359.

CONFLICT OF INTEREST

The authors declare that they have no known competing financial interests and private or personal relationships that could have appeared to influence on the work presented in this article.

OPEN ACCESS

This article is licensed under a Creative Commons Attribution 4.0 International License, which permits use, sharing, adaptation, distribution and reproduction in any medium or format, as long as you give appropriate credit to the original author(s) and the source, provide a link to the Creative Commons licence, and indicate if changes were made. The images or other third party material in this article are included in the article's Creative Commons licence, unless indicated otherwise in a credit line to the material. If material is not included in the article's Creative Commons licence and your intended use is not permitted by statutory regulation or exceeds the permitted use, you will need to obtain permission directly from the copyright holder. To view a copy of this licence, visit <http://creativecommons.org/licenses/by/4.0/>.

REFERENCES

1. P.B. Price: *Philos. Mag.*, 1960, vol. 57, pp. 873–86.
2. K.H. Adams, T. Vreeland Jr., and D.S. Wood: *Mater. Sci. Eng.*, 1967, vol. 2(1), pp. 37–47.
3. S. Yoshida and N. Nagata: *Trans. Jpn. Inst. Met.*, 1967, vol. 9(2), pp. 110–19.
4. K.H. Adams, R.C. Blish, and T. Vreeland Jr.: *Mater. Sci. Eng.*, 1967, vol. 2(4), pp. 201–07.
5. P.B. Price and F.P. Bowden: *Proc. R. Soc. Lond. Ser. A*, 1961, vol. 260(130), pp. 251–62.
6. S. Jin, S. Xie, M.J. Burek, Z. Jahed, and T.Y. Tsui: *J. Mater. Res.*, 2012, vol. 27, pp. 2140–47.
7. L. Cauvin, B. Raghavan, S. Bouvier, X. Wang, and F. Meraghni: *Mater. Sci. Eng. A*, 2018, vol. 729, pp. 109–18.
8. D.H. Lassila, M.M. LeBlanc, and J.N. Florando: *Metall. Mater. Trans. A*, 2006, vol. 38, pp. 2024–32.
9. J.N. Florando, M. Rhee, A. Arsenlis, and M.M. LeBlanc: *Philos. Mag. Lett.*, 2016, vol. 86(12), pp. 795–805.
10. A.R. Gokhale, R. Sarvesha, R. Prasad, S.S. Singh, and J. Jain: *J. Eng. Mater. Technol.*, 2019, <https://doi.org/10.1115/1.4044438>.
11. R.R. Tohid and S.J. Bull: *Int. J. Mater. Res.*, 2007, vol. 98(5), pp. 353–59.
12. J.J. Vlassak and W.D. Nix: *J. Mech. Phys. Solids*, 1994, vol. 42(8), pp. 1223–45.
13. N.P.T. Nguyen, F. Abbès, B. Abbès, and Y. Li: in *Proceedings of the International Conference on Advances in Computational Mechanics 2017*, 1st ed., Springer, Phu Quoc Island, Vietnam, 2017, pp. 157–69.
14. P.T.N. Nguyen, F. Abbès, B. Abbès, J.S. Lecomte, and C. Schuman: *IOP Conf. Ser.: Mater. Sci. Eng.*, 2019, vol. 540, p. 012011. <https://doi.org/10.1088/1757-899X/540/1/012011>.
15. R. Sarvesha, A. Gokhale, K. Kumar, N.K. Sharma, J. Jain, and S.S. Singh: *Mater. Sci. Eng. A*, 2020, vol. 776, p. 139064.
16. J.H. Liu, C.X. Huang, S.D. Wu, and Z.F. Zhang: *Mater. Sci. Eng. A*, 2008, vol. 490, pp. 117–25.
17. S. Pathak, J. Schaffer, and S.R. Kalidindi: *Scripta Mater.*, 2009, vol. 60(6), pp. 439–42.
18. G. Nayyeri, W.J. Poole, C.W. Sinclair, and S. Zaefferer: *Scripta Mater.*, 2017, vol. 137, pp. 119–22.
19. G. Nayyeri, W.J. Poole, C.W. Sinclair, and S. Zaefferer: *Scripta Mater.*, 2018, vol. 156, pp. 37–41.
20. R. Sánchez-Martín, M.T. Pérez-Prado, J. Segurado, J. Bohlen, I. Gutiérrez-Urrutia, J. Llorca, and J.M. Molina-Aldareguia: *Acta Mater.*, 2014, vol. 71, pp. 283–92.
21. T. Guo, F. Siska, J. Cheng, and M. Barnett: *J. Alloys Compd.*, 2018, vol. 731, pp. 620–30.
22. F. Siska, T. Guo, L. Stratila, J. Cizek, and M.R. Barnett: *Comput. Mater. Sci.*, 2017, vol. 126, pp. 393–99.
23. H.S. Somekawa and C.A. Schuh: *Metall. Mater. Trans. A*, 2016, vol. 47, pp. 3227–34.
24. H. Somekawa, T. Tsuru, A. Singh, S. Miura, and C.A. Schuh: *Acta Mater.*, 2017, vol. 139, pp. 21–29.
25. H. Kitahara, T. Mayama, K. Okumura, Y. Tadano, M. Tsushida, and S. Ando: *Acta Mater.*, 2014, vol. 78, pp. 290–300.
26. C. Zambaldi, C. Zehnder, and D. Raabe: *Acta Mater.*, 2015, vol. 91, pp. 267–88.
27. H. Bei, Y.F. Gao, S. Shim, E.P. George, and G.M. Pharr: *Phys. Rev. B*, 2008, <https://doi.org/10.1103/PhysRevB.77.060103>.
28. M. Goken, R. Sakidja, W.D. Nix, and J.H. Perepezko: *Mater. Sci. Eng. A*, 2001, vol. 319–321, pp. 902–08.
29. D.A. Lucca, M.J. Klopstein, R. Ghisleni, and G. Cantwell: *CIRP Ann.*, 2001, vol. 51(1), pp. 483–86.
30. D. Catoor, Y.F. Gao, J. Geng, M.J.N.V. Prasad, E.G. Herbert, K.S. Kumar, G.M. Pharr, and E.P. George: *Acta Mater.*, 2013, vol. 61(8), pp. 2953–65.
31. W.C. Oliver and G.M. Pharr: *J. Mater. Res.*, 1992, vol. 7, pp. 1564–83.
32. K. Miyahara, S. Matsuoka, and N. Nagashima: *JSME Int. J. Ser. A*, 1998, vol. 41(4), pp. 562–68.
33. A. Gouldstone, H.J. Koh, K.Y. Zeng, A.E. Giannakopoulos, and S. Suresh: *Acta Mater.*, 2000, vol. 48(9), pp. 2277–95.
34. S. Pathak, D. Stojakovic, R. Doherty, and S.R. Kalidindi: *J. Mater. Res.*, 2009, vol. 24, pp. 1142–55.
35. S.R. Kalidindi and S. Pathak: *Acta Mater.*, 2008, vol. 56, pp. 3523–32.
36. S. Pathak, J.L. Riesterer, S.R. Kalidindi, and J. Michler: *Appl. Phys. Lett.*, 2014, vol. 105, p. 161913.
37. D.C. Miller, M.J. Talmage, and K. Gall: *J. Mater.*, 2006, vol. 21(10), pp. 2480–92.
38. S. Kucharski and S. Woźniacka: *Metall. Mater. Trans. A*, 2019, vol. 50, pp. 2139–54.
39. C.A. Schuh: *Mater. Today*, 2006, vol. 9(5), pp. 32–40.
40. C.A. Schuh and A.C. Lund: *J. Mater. Res.*, 2004, vol. 19, pp. 2152–58.

41. G. Nayyeri, W.J. Poole, C.W. Sinclair, S. Zaefferer, P.J. Konijnenberg, and C. Zambaldi: *Mater. Sci. Eng. A*, 2016, vol. 670, pp. 132–45.
42. E.M. Allen, M. Moradi, and M.R. Maughan: *J. Mater. Res.*, 2021, vol. 36, pp. 2915–25.
43. A.M. Minor, S.A.S. Asif, Z. Shan, E.A. Stach, E. Cyrankowski, T.J. Wyrobek, and O.L. Warren: *Nat. Mater.*, 2006, vol. 5, pp. 697–702.
44. A.C. Lund, A.M. Hodge, and C.A. Schuh: *Appl. Phys. Lett.*, 2004, vol. 85, pp. 1362–64.
45. M.R. Maughan, A.A. Leonard, D.D. Stauffer, and D.F. Bahr: *Philos. Mag.*, 2017, vol. 97(22), pp. 1902–20.
46. M.R. Maughan and D.F. Bahr: *Mater. Res. Lett.*, 2015, vol. 3(1), pp. 58–64.
47. Y.L. Chiu and A.H.W. Ngan: *Acta Mater.*, 2002, vol. 50, pp. 1599–1611.
48. S. Kucharski, S. Stupkiewicz, and H. Petryk: *Exp. Mech.*, 2014, vol. 54, pp. 957–69.
49. S. Jiapeng, L. Cheng, J. Han, A. Ma, and L. Fang: *Sci. Rep.*, 2017, <https://doi.org/10.1038/s41598-017-11130-2>.
50. L. Chang and L.C. Zhang: *Acta Mater.*, 2009, vol. 57(7), pp. 2148–53.
51. T. Vodenitcharova and L.C. Zhang: *Int. J. Solids Struct.*, 2004, vol. 41(18–19), pp. 5411–24.
52. T.F. Page, W.C. Oliver, and C.J. McHargue: *J. Mater. Res.*, 1992, vol. 7, pp. 450–73.
53. M.J. Cordill, N.R. Moody, and W.W. Gerberich: *MRS Online Proc. Libr.*, 2006, <https://doi.org/10.1557/PROC-976-0976-EE09-05>.
54. M.H. Yoo: *Metall. Mater. Trans. A*, 1981, vol. 12, pp. 409–18.
55. M.H. Yoo and C. Wei: *J. Appl. Phys.*, 1967, vol. 38, pp. 2974–76.

Publisher's Note Springer Nature remains neutral with regard to jurisdictional claims in published maps and institutional affiliations.